

Planck Early Results: Dust in the diffuse interstellar medium and the Galactic halo

Planck Collaboration: A. Abergel⁴⁴, P. A. R. Ade⁶⁷, N. Aghanim⁴⁴, M. Arnaud⁵⁴, M. Ashdown^{52,73}, J. Aumont⁴⁴, C. Baccigalupi⁶⁵, A. Balbi²⁶, A. J. Banday^{71,6,59}, R. B. Barreiro⁴⁹, J. G. Bartlett^{3,50}, E. Battaner⁷⁵, K. Benabed⁴⁵, A. Benoît⁴⁵, J.-P. Bernard^{71,6}, M. Bersanelli^{24,39}, R. Bhatia³¹, K. Blagrove⁵, J. J. Bock^{50,7}, A. Bonaldi³⁵, J. R. Bond⁵, J. Borrill^{58,68}, F. R. Bouchet⁴⁵, F. Boulanger⁴⁴, M. Bucher³, C. Burigana³⁸, P. Cabella²⁶, C. M. Cantalupo⁵⁸, J.-F. Cardoso^{55,3,45}, A. Catalano^{3,53}, L. Cayón¹⁷, A. Challinor^{74,52,8}, A. Chamballu⁴², L.-Y. Chiang⁴⁶, C. Chiang¹⁶, P. R. Christensen^{62,27}, D. L. Clements⁴², S. Colombi⁴⁵, F. Couchot⁵⁷, A. Coulais⁵³, B. P. Crill^{50,63}, F. Cuttaia³⁸, L. Danese⁶⁵, R. D. Davies⁵¹, R. J. Davis⁵¹, P. de Bernardis²³, G. de Gasperis²⁶, A. de Rosa³⁸, G. de Zotti^{35,65}, J. Delabrouille³, J.-M. Delouis⁴⁵, F.-X. Désert⁴¹, C. Dickinson⁵¹, S. Donzelli^{39,47}, O. Doré^{50,7}, U. Dörl⁵⁹, M. Douspis⁴⁴, X. Dupac³⁰, G. Efstathiou⁷⁴, T. A. Enßlin⁵⁹, H. K. Eriksen⁴⁷, F. Finelli³⁸, O. Forni^{71,6}, M. Frailis³⁷, E. Franceschi³⁸, S. Galeotta³⁷, K. Ganga^{3,43}, M. Giard^{71,6}, G. Giardino³¹, Y. Giraud-Héraud³, J. González-Nuevo⁶⁵, K. M. Górski^{50,77}, S. Gratton^{52,74}, A. Gregorio²⁵, A. Gruppuso³⁸, F. K. Hansen⁴⁷, D. Harrison^{74,52}, G. Helou⁷, S. Henrot-Versillé⁵⁷, D. Herranz⁴⁹, S. R. Hildebrandt^{7,56,48}, E. Hivon⁴⁵, M. Hobson⁷³, W. A. Holmes⁵⁰, W. Hovest⁵⁹, R. J. Hoyland⁴⁸, K. M. Huffenberger⁷⁶, A. H. Jaffe⁴², G. Joncas¹¹, A. Jones⁴⁴, W. C. Jones¹⁶, M. Juvela¹⁵, E. Keihänen¹⁵, R. Keskitalo^{50,15}, T. S. Kisner⁵⁸, R. Kneissl^{29,4}, L. Knox¹⁹, H. Kurki-Suonio^{15,33}, G. Lagache⁴⁴, J.-M. Lamarre⁵³, A. Lasenby^{73,52}, R. J. Laureijs³¹, C. R. Lawrence⁵⁰, S. Leach⁶⁵, R. Leonardi^{30,31,20}, C. Leroy^{44,71,6}, M. Linden-Vørnle¹⁰, F. J. Lockman³², M. López-Cañiegos⁴⁹, P. M. Lubin²⁰, J. F. Macías-Pérez⁵⁶, C. J. MacTavish⁵², B. Maffei⁵¹, D. Maino^{24,39}, N. Mandolesi³⁸, R. Mann⁶⁶, M. Maris³⁷, D. J. Marshall^{71,6}, P. Martin⁵, E. Martínez-González⁴⁹, S. Masi²³, S. Matarrese²², F. Matthai⁵⁹, P. Mazzotta²⁶, P. McGehee⁴³, P. R. Meinhold²⁰, A. Melchiorri²³, L. Mendes³⁰, A. Mennella^{24,37}, M.-A. Miville-Deschênes^{44,5*}, A. Moneti⁴⁵, L. Montier^{71,6}, G. Morgante³⁸, D. Mortlock⁴², D. Munshi^{67,74}, A. Murphy⁶¹, P. Naselsky^{62,27}, F. Nati²³, P. Natoli^{26,2,38}, C. B. Netterfield¹³, H. U. Nørgaard-Nielsen¹⁰, F. Novello⁴⁴, D. Novikov⁴², I. Novikov⁶², I. J. O'Dwyer⁵⁰, S. Osborne⁷⁰, F. Pajot⁴⁴, R. Paladini^{69,7}, F. Pasian³⁷, G. Patanchon³, O. Perdereau⁵⁷, L. Perotto⁵⁶, F. Perrotta⁶⁵, F. Piacentini²³, M. Piat³, D. Pinheiro Gonçalves¹³, S. Plaszczynski⁵⁷, E. Pointecouteau^{71,6}, G. Polenta^{2,36}, N. Ponthieu⁴⁴, T. Poutanen^{33,15,1}, G. Prézeau^{7,50}, S. Prunet⁴⁵, J.-L. Puget⁴⁴, J. P. Rachen⁵⁹, W. T. Reach⁷², M. Reinecke⁵⁹, C. Renault⁵⁶, S. Ricciardi³⁸, T. Riller⁵⁹, I. Ristorcelli^{71,6}, G. Rocha^{50,7}, C. Rosset³, M. Rowan-Robinson⁴², J. A. Rubiño-Martín^{48,28}, B. Rusholme⁴³, M. Sandri³⁸, D. Santos⁵⁶, G. Savini⁶⁴, D. Scott¹⁴, M. D. Seiffert^{50,7}, P. Shellard⁸, G. F. Smoot^{18,58,3}, J.-L. Starck^{54,39}, F. Stivoli⁴⁰, V. Stolyarov⁷³, R. Stompor³, R. Sudiwala⁶⁷, J.-F. Sygnet⁴⁵, J. A. Tauber³¹, L. Terenzi³⁸, L. Toffolatti¹², M. Tomasi^{24,39}, J.-P. Torre⁴⁴, M. Tristram⁵⁷, J. Tuovinen⁶⁰, G. Umana³⁴, L. Valenziano³⁸, P. Vielva⁴⁹, F. Villa³⁸, N. Vittorio²⁶, L. A. Wade⁵⁰, B. D. Wandelt^{45,21}, A. Wilkinson⁵¹, D. Yvon⁹, A. Zacchei³⁷, and A. Zonca²⁰

(Affiliations can be found after the references)

September 3, 2022

ABSTRACT

This paper presents the first results of comparison of *Planck* dust maps at 353, 545 and 857 GHz, along with *IRAS* data at 3000 (100 μ m) and 5000 GHz (60 μ m), with Green Bank Telescope 21-cm observations of HI in 14 fields covering more than 800 square degrees at high Galactic latitude. The main goal of this study is to estimate the far-infrared to sub-millimetre emissivity of dust in the diffuse local interstellar medium and in the intermediate-velocity and high-velocity clouds of the Galactic halo.

Galactic dust emission for fields with average column density lower than $2 \times 10^{20} \text{ cm}^{-2}$ is well correlated with 21-cm emission because in such diffuse areas the hydrogen is predominantly in the neutral atomic phase. The residual emission in these fields, once the HI-correlated emission is removed, is consistent with the expected statistical properties of the cosmic infrared background fluctuations.

The brighter fields in our sample with an average column density greater than $2 \times 10^{20} \text{ cm}^{-2}$ show significant excess dust emission compared to the HI column density. Regions of excess lie in organized structures that suggest the presence of hydrogen in molecular form, though they are not always correlated with CO emission. In the higher N_{HI} fields the excess emission at 857 GHz is about 40% of that coming from the HI, but over all the high latitude fields surveyed the molecular mass fraction is about 10%.

Dust emission from intermediate-velocity clouds is detected by this correlation analysis with high significance. Its spectral properties are consistent with, compared to the local ISM values, significantly hotter dust ($T \sim 20 \text{ K}$), lower emission cross-section and a relative abundance of very small grains to large grains about four times higher. These results are consistent with expectations for clouds that are part of the Galactic fountain in which there is dust shattering and fragmentation.

Correlated dust emission in high-velocity clouds is detected only marginally at the 1 to 3.5 σ level. It has a significantly lower emissivity at 857 GHz (a factor of ten compared to the local ISM), in accordance with the lower metallicity of these clouds.

Unexpected anti-correlated variations of the dust temperature and emission cross section per H atom are identified in the local ISM and IVCs, a trend that continues into molecular environments. This suggests that dust growth through aggregation, seen in molecular clouds and then in circumstellar disks leading to the formation of planetesimals, is active much earlier in the cloud condensation and star formation processes.

Key words. Methods: data analysis – dust – local interstellar matter – Galaxy: halo – Submillimeter: ISM – Infrared: ISM

1. Introduction

*Planck*¹ (Tauber et al. 2010; Planck Collaboration 2011a) is the third-generation space mission to measure the anisotropy of the

¹ *Planck* (<http://www.esa.int/Planck>) is a project of the European Space Agency (ESA) with instruments provided by two scientific con-

* Corresponding author: M.-A. Miville-Deschênes, mamd@ias.u-psud.fr

cosmic microwave background (CMB). It observes the sky in nine frequency bands covering 30–857 GHz with high sensitivity and angular resolution from 31' to 5'. The Low Frequency Instrument (LFI; [Mandolesi et al. 2010](#); [Bersanelli et al. 2010](#); [Mennella et al. 2011](#)) covers the 30, 44, and 70 GHz bands with amplifiers cooled to 20 K. The High Frequency Instrument (HFI; [Lamarre et al. 2010](#); [Planck HFI Core Team 2011a](#)) covers the 100, 143, 217, 353, 545, and 857 GHz bands with bolometers cooled to 0.1 K. *Planck*'s sensitivity, angular resolution, and frequency coverage make it a powerful instrument for Galactic and extragalactic astrophysics as well as cosmology. This paper presents the first results of the analysis of *Planck* observations of the diffuse interstellar medium (ISM) at high Galactic latitude.

From the pioneering work of Spitzer and Field ([Spitzer 1956](#); [Field 1965](#); [Field et al. 1969](#)), observations of the diffuse ISM including intermediate and high-velocity clouds (IVCs and HVCs) have been the basis of our understanding of the dynamical interplay between ISM phases and the disk-halo connection in relation to star formation. Space-based observations have given us spectacular perspectives on the diffuse Galactic infrared emission, which highlight the role of dust not only as a tracer of the diffuse ISM but also as an agent in its evolution.

The *IRAS* images revealed the intricate morphology of infrared cirrus ([Low et al. 1984](#)) and prompted a wide range of observations. The cirrus is inferred to be inhomogeneous turbulent dusty clouds with dense CO-emitting gas intermixed with cold (CNM) and warm (WNM) neutral atomic gas and also diffuse H_2 . From imaging by *Spitzer*, and very recently *Herschel*, their structure is now known to extend to much smaller angular scales than observable at the *IRAS* resolution ([Ingalls et al. 2004](#); [Martin et al. 2010](#); [Miville-Deschênes et al. 2010](#)). Observations from *IRAS*, *ISO*, and *Spitzer* have also been used to characterize changes in the spectral energy distribution (SED) from mid to far-IR wavelengths, which have been interpreted as evidence for variations in the abundance of small stochastically-heated dust particles. The correlation with HI spectroscopic data suggests that interstellar turbulence may play a role in changing the dust size distribution ([Miville-Deschênes et al. 2002a](#)).

Since the breakthrough discoveries made with the Cosmic Background Explorer (*COBE*), the study of dust and the diffuse ISM structure has also become an integral part of the analysis of the Cosmic Microwave Background (CMB) and the Cosmic Infrared extragalactic Background (CIB). Our ability to model the spatial and spectral distribution of the infrared cirrus emission could limit our ability to achieve the cosmological goals of *Planck*, as well as of present balloon-borne and ground-based CMB experiments.

Accordingly, the *Planck* survey was designed to provide an unprecedented view of the structure of the diffuse ISM and its dust content. *Planck* extends to sub-millimeter (submm) wavelengths the detailed mapping of the infrared cirrus by the *IRAS* survey. Its sensitivity to faint Galactic cirrus emission is limited only by the astrophysical noise associated with the anisotropy of the CIB. The *Planck* survey is a major step forward from *IRAS* for two main reasons. First, by extending the spectral coverage to submm wavelengths, *Planck* allows us to probe the full SED of thermal emission from the large dust grains that are the bulk of the dust mass. Second, the dust temperatures obtained via submm SEDs also help us to disentangle the effects of dust

column density, dust heating and dust emission cross section on the brightness of the dust emission.

The scientific motivation of this paper is to trace the structure of the diffuse ISM, including its elusive diffuse H_2 component, H^+ components, and the evolution of interstellar dust grains within the local ISM and the Galactic halo. We analyze the *Planck* data in selected fields which cover the full range of hydrogen column densities from high Galactic latitude cirrus, observed away from dark molecular clouds such as, e.g., Taurus ([Planck Collaboration 2011u](#)). Some of these fields have been selected such that IVCs and/or HVCs have a major contribution to the total hydrogen column density. For all of our fields, we have deep 21-cm spectroscopic observations obtained with the Green Bank Telescope (GBT, [Martin et al. 2011](#)). Our data analysis makes use of, and explores, the dust/gas correlation by spatially correlating *Planck* and *IRAS* data with HI observations. More specifically our study extends previous work on the diffuse ISM SED carried out with 7" resolution FIRAS data ([Boulanger et al. 1996](#)) or with 5' resolution 100 μm *IRAS* data ([Reach et al. 1998](#)).

The paper is organized as follows. In §2 we describe the 21-cm data and the construction of the column density map for each HI component. In §3 we describe the *Planck* and *IRAS* data. Section 4 describes the main analysis of the paper: the determination of the HI emissivities from 353 to 5000 GHz (60 to 850 μm). Results are presented in §5 followed by a discussion of some implications in §6. Conclusions wrap up the paper in §7.

2. 21-cm data

2.1. The Green Bank Telescope cirrus survey

The 21-cm HI spectra exploited here were obtained with the 100-meter Green Bank Telescope (GBT) over the period 2005 to 2010. Details of this high-latitude survey are presented by [Martin et al. \(2011\)](#). The adopted names, central coordinates, and sizes of the 14 GBT fields are given in Table A.1. The total area mapped is about 825 square degrees.

The spectra were taken with on-the-fly mapping. The primary beam of the GBT at 21 cm has a full-width half-maximum (FWHM) of 9.1', and so the integration time (4 s) and telescope scan rate were chosen to sample every 3.5', more finely than the Nyquist interval, 3.86'. The beam is only slightly broadened to 9.4' in the in-scan direction. Scans were made moving the telescope in one direction (Galactic longitude or Right Ascension), with steps of 3.5' in the orthogonal coordinate direction before the subsequent reverse scan.

Data were recorded with the GBT spectrometer by in-band frequency switching yielding spectra with a velocity coverage $-450 \leq v_{LSR} \leq +355$ km s⁻¹ at a resolution of 0.80 km s⁻¹. Spectra were calibrated, corrected for stray radiation, and placed on a brightness temperature (T_b) scale as described in [Blagrove et al. \(2010\)](#); [Boothroyd et al. \(2011\)](#); [Martin et al. \(2011\)](#). A third-order polynomial was fit to the emission-free regions of the spectra to remove any residual instrumental baseline. The spectra were gridded on the equiareal SFL (Sanson-Flamsteed - [Calabretta & Greisen \(2002\)](#)) projection to produce a data cube. Some regions were mapped two or three times.

With the broad spectral coverage, all HI components from local gas to HVCs are accessible. The total column density N_{HI} ranges from 0.6×10^{20} cm⁻² in the SP field to 10×10^{20} cm⁻² in POL and NEP; the average column density per field ranges from 1.1×10^{20} cm⁻² in Bootes to 6.3×10^{20} cm⁻² in POL.

sortia funded by ESA member states (in particular the lead countries France and Italy), with contributions from NASA (USA) and telescope reflectors provided by a collaboration between ESA and a scientific consortium led and funded by Denmark.

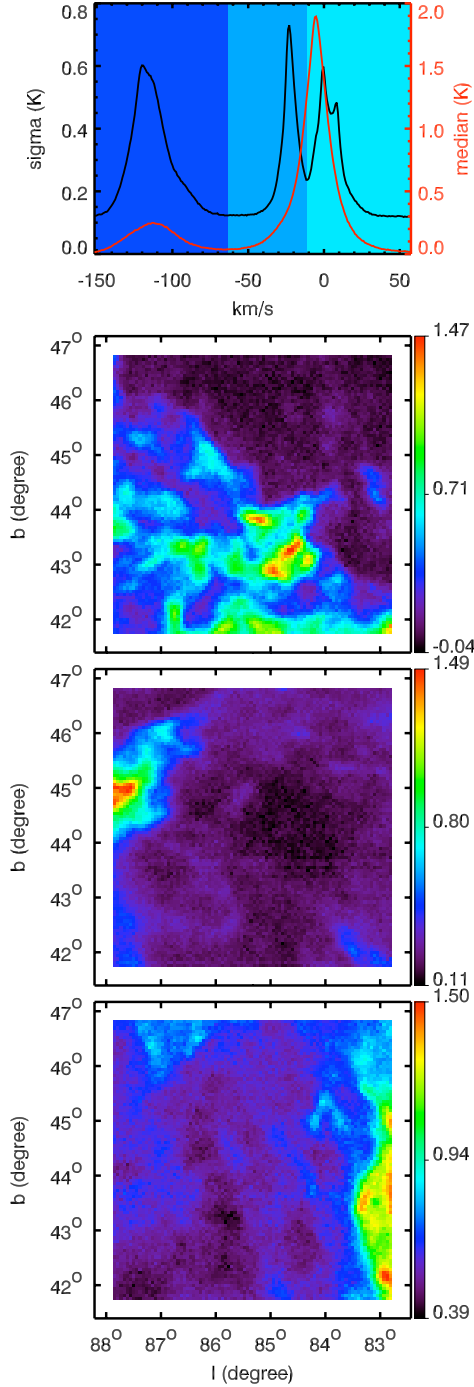


Fig. 1. HI components in the N1 field. From bottom to top: local, IVC and HVC. Units are 10^{20} cm^{-2} . The top panel shows the median 21-cm spectrum (red) and the standard-deviation spectrum (black); the shaded backgrounds show the velocity ranges used to estimate local (turquoise), IVC (light blue) and HVC (royal blue) components.

2.2. The HI components

The high Galactic latitude sky offers the opportunity to probe clouds with very different physical conditions, from the diffuse ISM close to the Sun to the Galactic halo with IVCs and HVCs. Here we use the velocity information provided by the 21-cm

GBT data to map the HI column density of different clouds superimposed in each field. For convenience we have separated the emission into three components for each field: local ISM, IVC, and HVC.

The selection of the velocity range for each component is based on inspection of the median 21-cm spectrum and the spectrum made from the standard deviation of each channel map. An example of these two spectra for the N1 field is shown in the top panel of Fig. 1. The red and black lines show the median and standard deviation of the brightness temperature as a function of velocity. Each HI component is expected to be composed of the two thermal phases: the CNM and WNM. In term of the 21 cm emission, the observed spectrum shows narrow features coming from the colder gas on top of a broad and smooth background coming from the warm gas. The median spectrum is sensitive to the whole 21-cm emission; in the case of the N1 field it shows a wide component centered near -5 km s^{-1} which reflects the presence of broad WNM emission from both the local and IVC components. In this case, these two components are close enough in velocity that their WNM emissions overlap. On the other hand, the standard-deviation spectrum shows a clear separation between local and IVC gas at -11 km/s . This arises because the CNM shows more small scale spatial structure (i.e., brightness contrast) in a given channel map than the WNM and because CNM spectral features in both local and IVC components are more localized in velocity due to their smaller (thermal and turbulent) broadening. Therefore, in velocity channels where the CNM contribution is more important the brightness fluctuation level is increased, which results in a greater standard deviation for these channels.

Because the standard-deviation spectrum is sensitive to the (CNM) structure, and so less sensitive to the warmer gas, we adopt it to separate more easily the local emission from the IVC emission. The three shaded backgrounds in Fig. 1 show the velocity ranges used to calculate the HI column density of the three components in this field.

The brightness temperature of each velocity channel was converted to column density, assuming an opacity correction for HI gas with a constant spin temperature T_s , to provide an estimate of the total HI column density of each component:

$$N_{HI}(x, y) = A \times T_s \sum_v -\ln\left(1 - \frac{T_b(x, y, v)}{T_s}\right) \Delta v \quad (1)$$

where $A = 1.823 \times 10^{18} \text{ cm}^{-2} (\text{K km s}^{-1})^{-1}$. In the optically-thin case (assuming $T_s \gg T_b$) this reduces to

$$N_{HI}(x, y) = A \sum_v T_b(x, y, v) \Delta v. \quad (2)$$

We used $T_s = 80 \text{ K}$ which is the collisional temperature found from the H_2 observations for column densities near 10^{20} cm^{-2} (Gillmon et al. 2006; Wakker 2006). It is also similar to the average HI spin temperature (column density weighted) found by Heiles & Troland (2003). T_s will be higher for the WNM, but for these high latitude diffuse lines of sight $T_b \ll 80 \text{ K}$ for the broad WNM lines, and so adopting the wrong T_s is of no consequence. For most fields the correction is less than 3% compared to the optically-thin assumption. Indeed very few of our 21-cm spectra reach brightness temperatures above 40 K - only 3% of the spectra in POL field, the brightest one in the sample. For these “extreme” cases the opacity correction to the column density reaches 35%.

The three bottom panels of Fig. 1 show the column density map of the N1 field, in units of 10^{20} cm^{-2} . The average HI col-

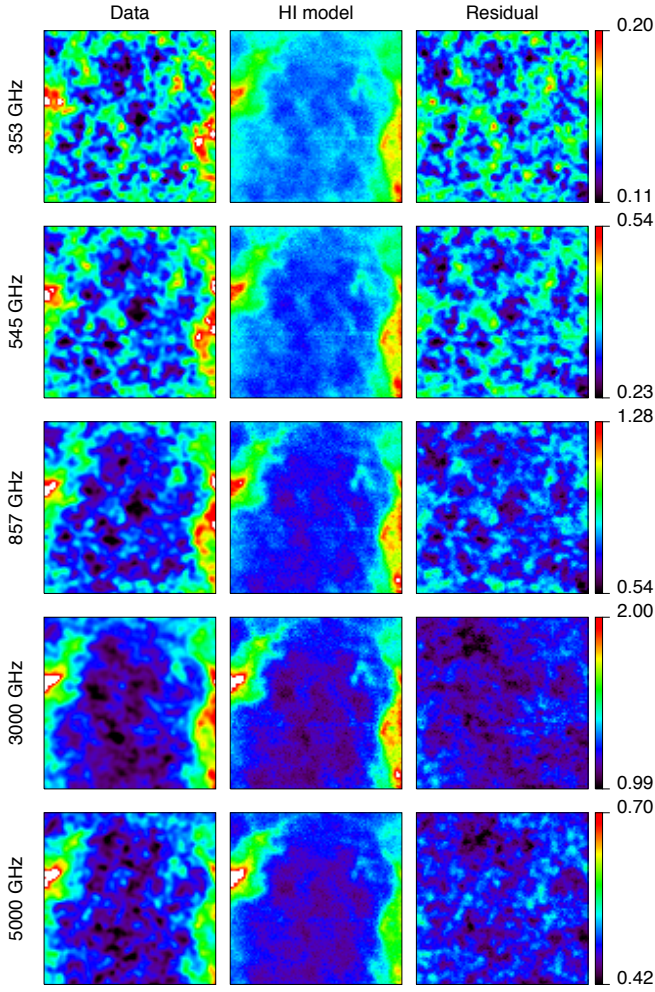


Fig. 2. Dust/gas correlation in the N1 field: *Planck* and *IRAS* raw maps (left column), the portion linearly correlated with N_{HI} (middle), and the residual emission (right). Units are MJy sr⁻¹.

umn densities of the local, IVC, and HVC components for all fields are compiled in Table A.1.

2.3. Uncertainties in N_{HI}

The main analysis presented here relies on a correlation analysis between far-infrared/submm brightness and N_{HI} of the components deduced from 21-cm emission. In order to estimate properly the uncertainties of the deduced correlation coefficients, we need to evaluate the uncertainty of the values of N_{HI} for the HI components. The method described in Appendix A takes advantage of the fact that the GBT observations were obtained in two polarisations. The difference between these spectra gives a direct estimate of the uncertainty in each channel which can be integrated over the appropriate velocity ranges, providing a column density uncertainty for each HI component. The HI column density uncertainties, expressed in units of 10^{20} cm⁻², are given in Table A.1 for the three HI components of each field.

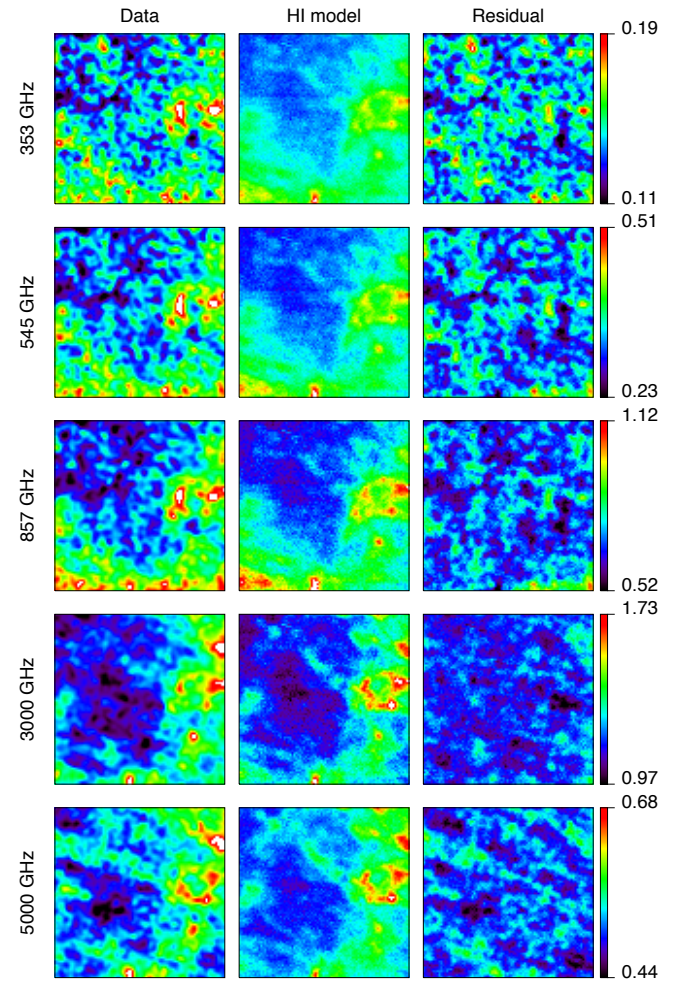


Fig. 3. Like Fig. 2, for field SP.

3. *Planck* and *IRAS*

3.1. Map construction

Our analysis uses infrared to submm data at 3000 and 5000 GHz (100 and 60 μm , respectively) from *IRAS* (IRIS, [Miville-Deschênes & Lagache 2005](#)) and at 353, 545, and 857 GHz (850, 550, and 350 μm , respectively) from *Planck* (DR2 release; [Planck HFI Core Team 2011b](#)), beginning with maps in Healpix form ([Gorski et al. 2005](#)) with $n_{\text{side}} = 2048$ (pixel size of 1.7'). We concentrated here on the three highest frequencies of *Planck* to avoid the significant contamination from residual CMB fluctuations and interstellar emission other than thermal dust (CO, synchrotron, free-free and spinning dust).

To obtain infrared-submm maps corresponding to each GBT field we first projected each Healpix map, using the nearest neighbor method, onto SFL grids with a pixel size of 1.7'. Each grid was centered on a given GBT field with a size 10% larger in each direction in order to avoid edge effects in subsequent convolution. Each SFL map was then converted to MJy sr⁻¹ and point sources were removed and replaced by interpolation of the surrounding map². The map was then convolved to bring it to the GBT 9.4' resolution and finally projected, using bi-linear in-

² For *Planck* channels we removed only point sources identified in the ERCSC ([Planck Collaboration 2011c](#)). For *IRAS* maps we used

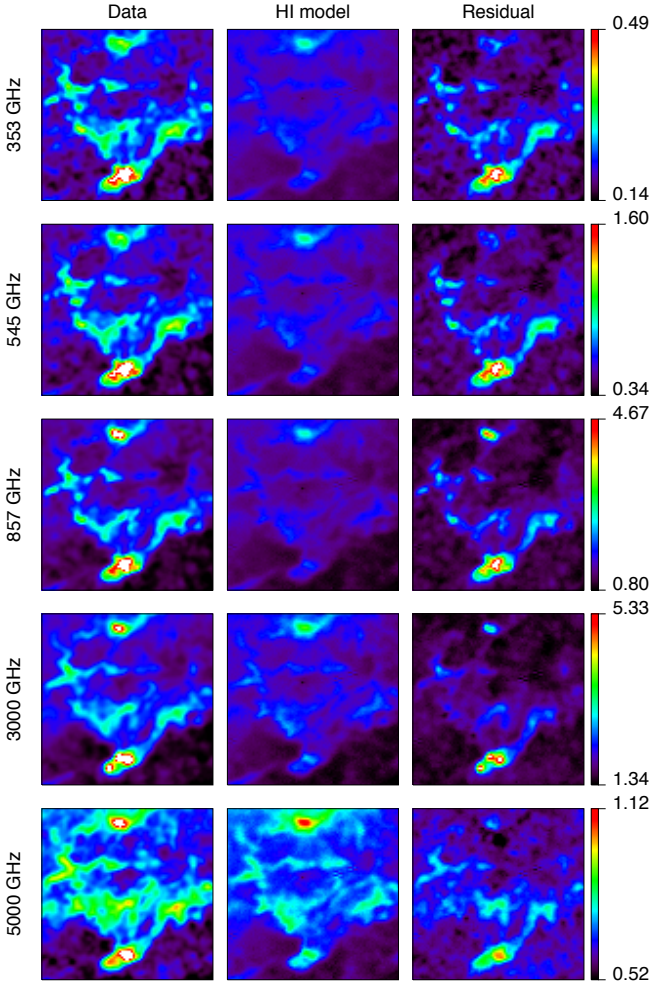


Fig. 4. Like Fig. 2, for the Draco field.

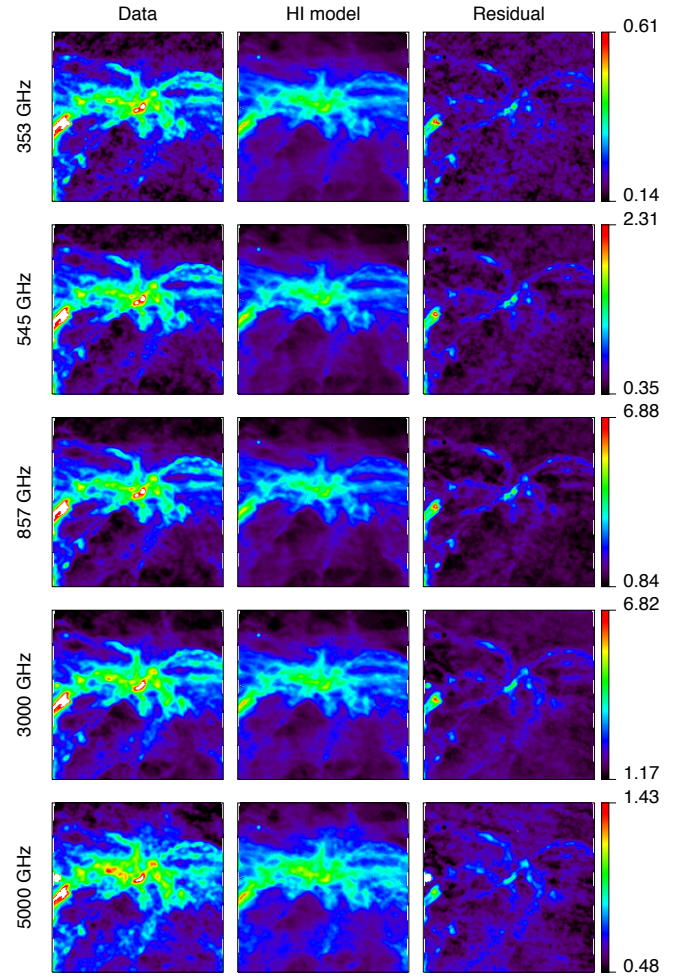


Fig. 5. Like Fig. 2, for the Spider field.

terpolation, on the actual GBT grid ($3.5''/\text{pixel}$). The *Planck* and *IRAS* maps for our fields are shown in Figures 2 to 5 and B.2 to B.11.

3.2. Dust brightness uncertainty

To estimate the noise level of the *Planck* and *IRAS* maps we used the method described in §5.1 of Miville-Deschênes & Lagache (2005). For both data sets we used the difference of maps of the same region of the sky obtained with different subsamples of the data. These difference maps, properly weighted by their coverage maps, provide an estimate of the statistical properties of the noise. For *Planck* the noise was estimated using the difference of the first and second half ring maps (Planck HFI Core Team 2011b). In the case of *IRAS*, each ISSA plate is the combination of up to three maps built from independent observations over the life of the satellite. We built difference maps from these three sets of maps. The procedure used to estimate the *Planck* and *IRAS* noise levels at the GBT resolution is detailed in Appendix B. The noise levels for each field and each frequency are given in Table B.1.

the source removal method described in Miville-Deschênes & Lagache (2005)

4. Dust-HI correlation

4.1. Model

Many studies, mostly using the *IRAS* and *COBE* data compared with various 21-cm surveys (Boulanger & Péroult 1988; Joncas et al. 1992; Jones et al. 1995; Boulanger et al. 1996; Arendt et al. 1998; Reach et al. 1998; Lockman & Condon 2005; Miville-Deschênes et al. 2005), have revealed the strong correlation between far-infrared/submm dust emission and 21-cm integrated emission W_{HI} ³ at high Galactic latitudes. In particular Boulanger et al. (1996) studied this relation over the whole high Galactic latitude sky. They reported a tight dust-HI correlation for $W_{\text{HI}} < 250 \text{ K km s}^{-1}$, corresponding to $N_{\text{HI}} < 4.6 \times 10^{20} \text{ cm}^{-2}$. For higher column densities the dust emission systematically exceeds that expected by extrapolating the correlation. Examining specific high Galactic latitude regions, Arendt et al. (1998) and Reach et al. (1998) found infrared excesses with respect to N_{HI} with a threshold varying from 1.5 to $5.0 \times 10^{20} \text{ cm}^{-2}$.

As shown in Martin et al. (2011), part of this excess is due to the effect of 21-cm self-absorption that produces a systematic underestimate of the column density when deduced with the optically thin assumption. Even though this effect is only at a few percent level in our case because of the low column densities,

³ equivalent to optically-thin HI column density

applying an opacity correction (see §2.2) helps limiting this systematic effect.

Most of the infrared/submm excess is usually attributed to dust associated with hydrogen in molecular form. This hypothesis is in accordance with UV absorption measurements that show a sudden increase of the H_2 absorption at $N_H = 3 - 5 \times 10^{20} \text{ cm}^{-2}$ (Savage et al. 1977; Gillmon et al. 2006), roughly the threshold for departure from the linear correlation between dust emission and N_{HI} . It is also observed that the pixels showing evidence of excess are spatially correlated and correspond to, or at least are in the vicinity of, known molecular clouds traced by CO emission. See also the discussion in §6.1.

A third source of this excess emission could be dust associated with the Warm Ionized Medium (WIM) but detection of this component is difficult (Arendt et al. 1998; Lagache et al. 2000) because there is no direct tracer of the ionized gas column density ($H\alpha$ depends on the square of the electron density and part of the structure seen in $H\alpha$ might be back-scattering of diffuse Galactic emission on dust and not photons produced within cirrus clouds (Witt et al. 2010)).

Finally, in the most diffuse regions of the high-latitude sky, the fluctuations of the CIB are a significant fraction of the brightness fluctuations in the infrared/submm. With a power spectrum flatter (k^{-1}) than that of the interstellar dust emission (k^{-3}) (Miville-Deschênes et al. 2002b; Miville-Deschênes et al. 2007; Lagache et al. 2007; Planck Collaboration 2011a), the CIB anisotropies contribute mostly at small angular scales, producing statistically homogeneous brightness fluctuations over any observed field, like an instrumental noise or the cosmic microwave background. Furthermore, because the CIB is unrelated to interstellar emission, the CIB fluctuations cannot be responsible for the excess of infrared emission seen at moderate to high N_{HI} column density.

In the analysis presented here we go a few steps further than the previous studies by 1) allowing for different dust emissivities for the local ISM, IVC, and HVC components, 2) applying an opacity correction to the 21-cm brightness temperatures in order to compute a more reliable N_{HI} , and 3) taking into account explicitly the CIB fluctuations which turn out to dominate the uncertainties in the derived emissivities.

In some fields like G86 with strong IVC emission, the distinctive morphology of the IVC column density map can be seen clearly in the line-of-sight integrated dust emission map (Martin et al. 1994), but even faint signals can be brought out by formal correlation analysis. We use the following model:

$$I_\nu(x, y) = \sum_{i=1}^3 \epsilon_\nu^i N_{\text{HI}}^i(x, y) + R_\nu(x, y) + Z_\nu \quad (3)$$

where $I_\nu(x, y)$ is the dust map at frequency ν (*IRAS* or *Planck*), ϵ_ν^i the emissivity of HI component i , and Z_ν is the zero level of the map. R_ν represents not only the contribution from noise in the data but also any emission in the *IRAS* and *Planck* bands that is not correlated with N_{HI} including the CIB anisotropies and potential dust emission coming from molecular or ionized gas. In this model we assume that the three HI components $N_{\text{HI}}^i(x, y)$ have a constant emissivity ϵ_ν^i over the field. Any spatial variations of the emissivity would also contribute to fluctuations in $R_\nu(x, y)$.

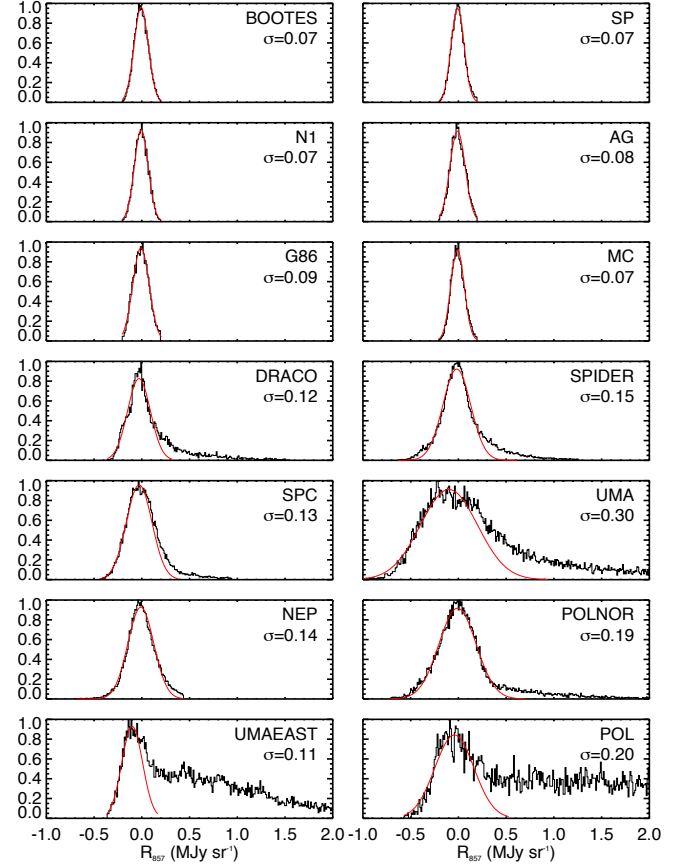


Fig. 6. Normalised PDF of the residual R_{857} of the dust-gas correlation at 857 GHz for each field after convergence of the masking procedure. The red curve is the result of a Gaussian fit ($\sigma \equiv \sigma_R$) to the lower, rising part of the PDF.

ν (GHz)	σ_S (MJy/sr)	$\sigma_{\text{noise}}^{\text{dust}}$ (MJy/sr)	$\sigma_{\text{noise}}^{\text{HI}}$ (MJy/sr)
353	0.0121 ± 0.0007	0.0060 ± 0.0012	0.0014 ± 0.0006
545	0.0383 ± 0.0022	0.0096 ± 0.0018	0.0056 ± 0.0023
857	0.0757 ± 0.0072	0.0097 ± 0.0019	0.0158 ± 0.0063
3000	0.0784 ± 0.0170	0.0280 ± 0.0042	0.0216 ± 0.0044
5000	0.0282 ± 0.0060	0.0146 ± 0.0016	0.0054 ± 0.0010

Table 1. Average of the standard deviations of the sky residual σ_S for the six fields with $\langle N_{\text{HI}} \rangle$ lower than $2 \times 10^{20} \text{ cm}^{-2}$ (AG, Bootes, G86, MC, N1, and SP). $\sigma_{\text{noise}}^{\text{dust}}$ is the average level of noise rms in the *IRAS* and *Planck* maps at the GBT resolution (i.e., noise level in maps convolved at $9.4'$) computed for the 14 fields. $\sigma_{\text{noise}}^{\text{HI}}$ gives the average GBT noise converted to MJy sr $^{-1}$ (see Eq. 8), for the 14 fields. All uncertainties are 1σ .

4.2. Estimating the dust emissivities

To estimate the parameters ϵ_ν^i and constant Z_ν we used the IDL function *regress* which, in the case of a general linear least-squares fit, solves the following equation (Press et al. 1995):

$$a = (A^T A)^{-1} \times (A^T b) \quad (4)$$

where a is the vector of the parameters ϵ_v^i and b is a vector of the N IRAS or *Planck* data points from the map, divided by their respective error:

$$b_i = \frac{I_v(i)}{\sigma_v}. \quad (5)$$

A is an $N \times M$ matrix that includes the N_{HI} values of the M HI components,

$$A_{ij} = \frac{N_{\text{HI}}^j(i)}{\sigma_v}. \quad (6)$$

Regress uses a Gaussian elimination method for the inversion.

For the model described in Eq. 3, the least-squares fit method provides a maximum-likelihood estimation of the parameters ϵ_v^i provided that the residual term $R_v(x, y)$ is uncorrelated with N_{HI}^i and its fluctuations are normally distributed (i.e., white noise). In addition, in order that the parameter estimates not be biased, the uncertainties on N_{HI}^i have to be comparatively small; we will show (see §4.5) that this last condition is satisfied for our data. On the other hand, we will also show that the residual term $R_v(x, y)$ is clearly not compatible with white noise. Even for the most diffuse fields in our sample, where the CIB fluctuations dominate the residual emission and the Probability Density Function (PDF) of $R_v(x, y)$ is normally distributed, the condition that there be no (not even chance) correlation with N_{HI} is not satisfied, because the power spectrum of the CIB is not white, but rather like k^{-1} (Planck Collaboration 2011n). For brighter fields, where spatial variation of the dust emission with respect to the HI templates is expected (due to the presence of molecules or spatial variation of dust properties), the residual is not even normally distributed.

To limit the influence of these effects, and in order to focus on estimating the dust emissivity of the HI components, we relied on a masking procedure to flag and remove obvious outliers with respect to the correlation, and on Monte-Carlo simulations to estimate the ϵ_v^i uncertainties and bias (see §4.5).

4.3. Masking

In order to limit the effect of lines of sight with significant “excess” dust emission that is not associated with HI gas, most previous authors used only data points with N_{HI} lower than a given threshold to stay in a regime of linear correlation. This thresholding was motivated by the fact that above some N_{HI} the extinction and self-shielding of H_2 are strong enough to limit photo-dissociation, whereas below the threshold the hydrogen is mostly atomic. The threshold depends sensitively on local gas density and temperature but for typical interstellar conditions for CNM gas ($n = 100 \text{ cm}^{-3}$, $T = 80 \text{ K}$, $G = 1$), it is about $N_{\text{HI}} = 2.5 \times 10^{20} \text{ cm}^{-2}$ (Reach et al. 1998). Others used a quadratic function for ϵ_v (Fixsen et al. 1998) based on the idea that the H_2 column density depends (at least dimensionally) on N_{HI}^2 (Reach et al. 1994). Both methods introduce a bias in the parameter estimation that is difficult to quantify.

Instead of applying an arbitrary cutoff in W_{HI} , Arendt et al. (1998) used an iterative method to exclude data points above a cut along lines perpendicular to the fit in order to arrive at a stable solution for ϵ_v . We used a similar approach by iteratively masking out data points that would produce a positively-skewed residual. That way we expect to keep pixels in the maps that correspond to lines of sight where the dust emission is dominated by the atomic HI components.

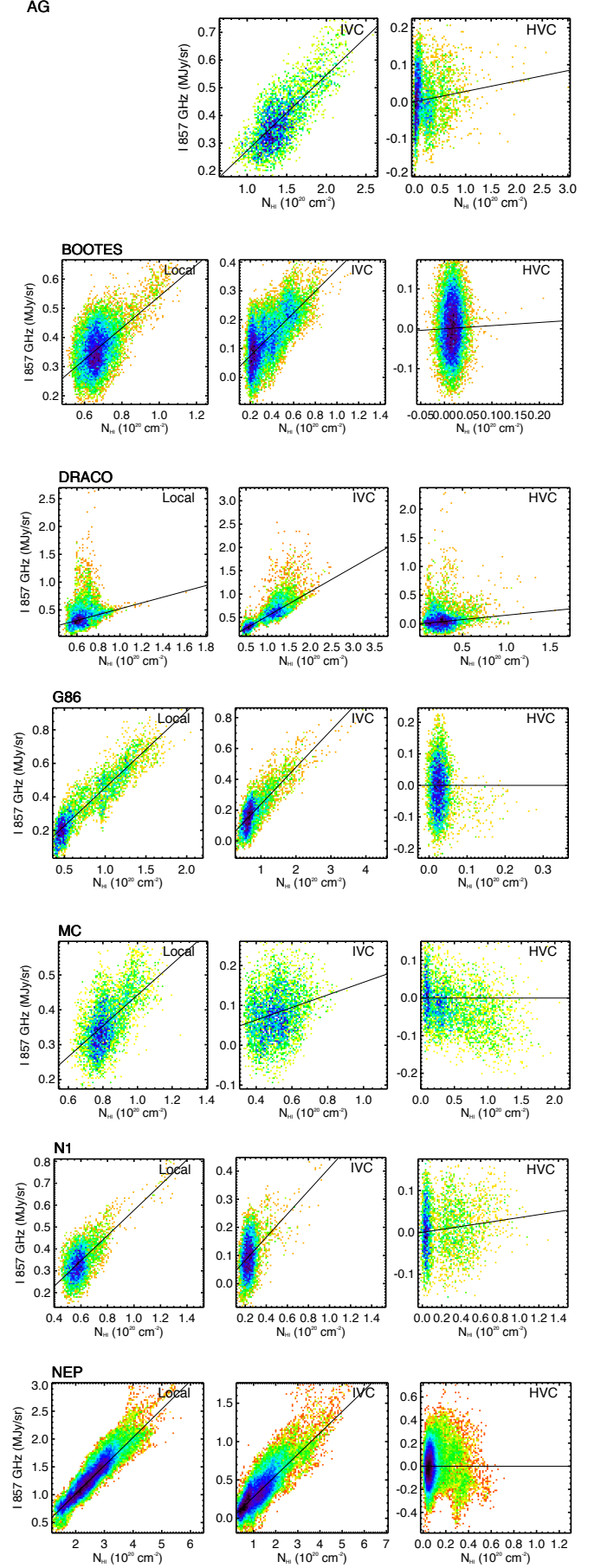


Fig. 7. I_{857} vs. N_{HI} scatter plots visualising the dust-gas correlation for each of the three HI component, across a row. For a given component, the remaining 857 GHz emission, once the contribution of the other two HI components has been removed, is plotted as a function of N_{HI} of that component. The color scale is linear in the density of data points. Note that field AG has no local gas component identified.

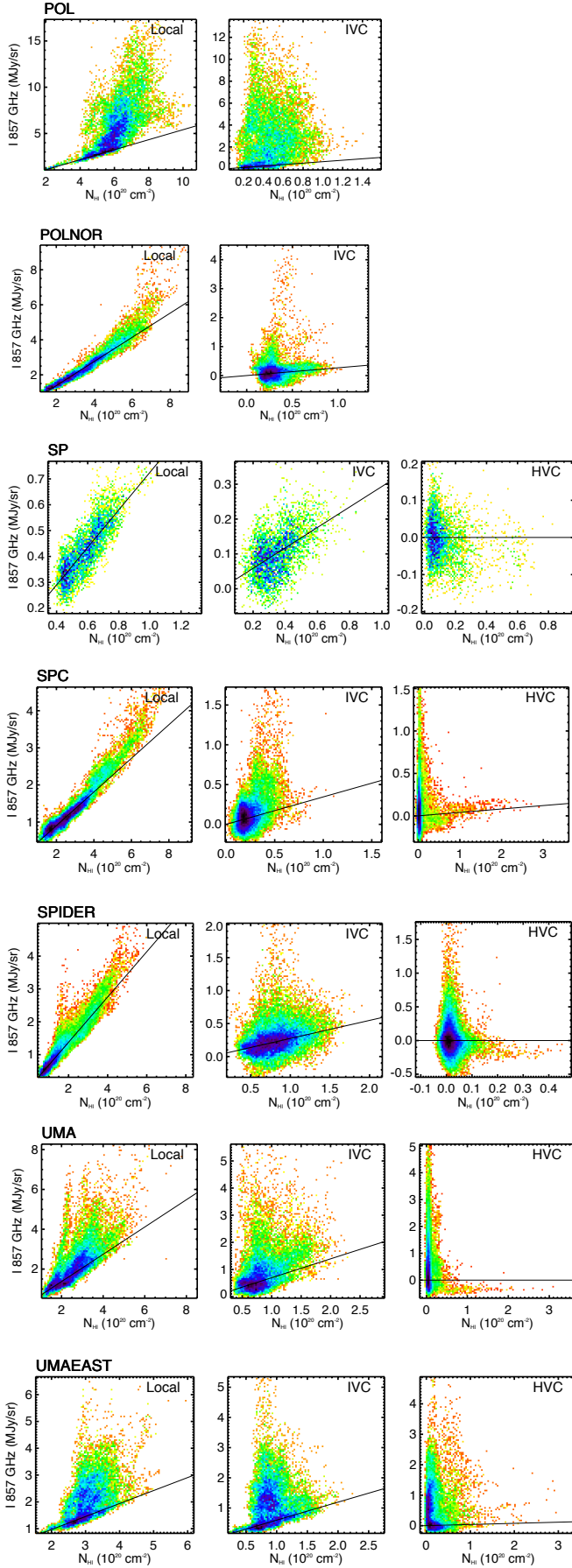


Fig. 8. Like Fig. 7. Note that the fields POL and POLNOR do not have an HVC component identified.

The first iteration of the process performed the multi-variate linear regression based on Equations 4 to 6 using only pixels where the total N_{HI} (i.e., the sum over the three HI components) is lower than $4 \times 10^{20} \text{ cm}^{-2}$. For further iterations this threshold was relaxed; but using it as a starting point ensures that the first estimate of the parameters is close to the ultimate solution.

The PDF of residual map, R , defined as

$$R_v(x, y) \equiv I_v(x, y) - \sum_{i=1}^3 \epsilon_v^i N_{\text{HI}}^i(x, y) - Z_v, \quad (7)$$

is then used to estimate the mask. We used the *Planck* 857-GHz channel because it has the best signal-to-noise ratio and is less sensitive than the *IRAS* channels to dust temperature induced emissivity variations.

As discussed above, the presence of dust emission associated with molecular gas can positively skew the PDF, and empirically the PDF of R_{857} is positively skewed for bright fields (see for instance NEP, DRACO or SPIDER in Fig. 6). On the other hand, for the most diffuse fields in our sample (AG, MC, N1, BOOTES, G86, SP) the PDF of R_{857} is very close to a Gaussian which suggests that the model described by Eq. 3 is the right one in such low column density regions.

To determine the set of pixels to be retained, we used a Gaussian fit to the lower, rising part of the PDF, up to the PDF maximum, and estimated the σ (see the red curves in Fig. 6). With the above motivation, we assume that the lower part of the PDF is representative of pixels where the fit works well (i.e., for these pixels the residual is normally distributed). Using the σ fit only to this part of the PDF, we apply a threshold in R_{857} by masking out all pixels with $R_{857} > 3 \times \sigma$ away from the mean. We iteratively recompute the parameters and mask to converge on a stable solution. The PDFs of R_{857} obtained at the end of the process are shown in Fig. 6.

For 8 out of 14 fields, the masking excluded less than 7% of the points (less than 1% for the six faintest fields). For these fields the mask has no significant effect on the estimated parameters. For the six other fields, the masking method excluded from 10 to 80% of the pixels. The masks for these six fields are shown in Fig. B.12. In these cases the masking has a significant effect on the result but we have checked that the estimated parameters are similar to the ones obtained with a $W_{\text{HI}} \leq 4 \times 10^{20} \text{ cm}^{-2}$ threshold. In fact the masking method used here allows us to keep pixels that would have been excluded by a simple W_{HI} thresholding even though they do not depart significantly from the linear correlation.

Table 2 provides the ϵ_v^i values for each field/component/frequency. In order to visualize the results, Figures 7 and 8 give scatter plots together with the line of slope ϵ_{857}^i for each component, field by field. Specifically, for each HI component i we plotted $I_v - \sum_{j \neq i} \epsilon_j N_{\text{HI}}^j - Z_v$ as a function of N_{HI}^i .

4.4. Statistics of the residual

Figures 2 to 5 and B.2 to B.11 show the *IRAS* and *Planck* maps, together with the HI correlated emission and the residual maps R_v for all our fields. For the six faintest fields (Figures 2, 3, B.2 to B.4 and B.6), the structure in the residuals is, even by visual inspection, clearly spatially correlated between frequencies, especially in the *Planck* bands. It is dominated by small scale structures with equally negative and positive brightness fluctuations. The structure of the residual for brighter fields (Figures 4, 5,

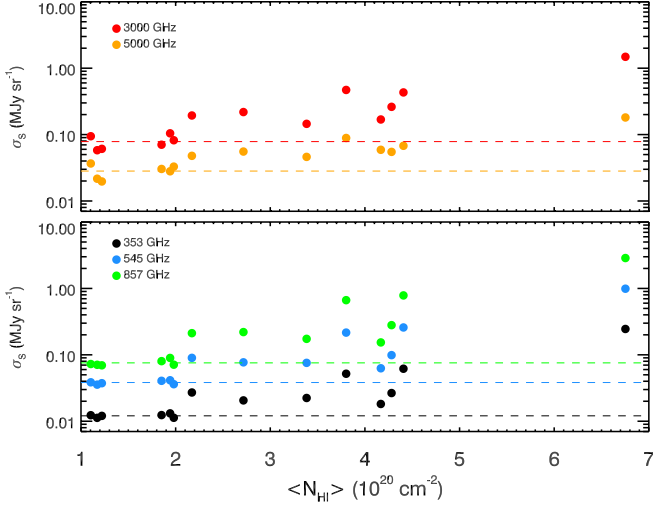


Fig. 9. Value of σ_S obtained from the standard deviation σ_R of the residual maps $R_v(x, y)$ from which contributions from the *IRAS* or *Planck* and the GBT noise were removed quadratically (see Eq. 8), plotted as a function of the average HI column density of each field. The dotted line is the average of σ_S for fields with $N_{HI} < 2 \times 10^{20} \text{ cm}^{-2}$.

B.5, B.7 to B.11) is also clearly correlated between frequencies but in these cases the residual is mostly positive (i.e., excesses with respect to the HI). These residuals also show larger coherent structures than in the fainter fields.

The rms (about the mean) of the residual R can be approximated as:

$$\sigma_R = \sqrt{\sigma_S^2 + (\sigma_{noise}^{dust})^2 + \sum_{i=1}^3 (\epsilon_v^i \delta N_{HI}^i)^2} \quad (8)$$

where noise in the *IRAS* or *Planck* data and that induced by uncertainties in N_{HI} are explicitly accounted for and σ_S includes all other contributions not in the model, including CIB anisotropies and dust emission associated with molecular gas. After quadratic subtraction of the contributions from *IRAS*, *Planck*, and GBT noise (see Appendices A and B) Fig. 9 shows the value of σ_S at each frequency, as a function of the average N_{HI} density for each field. For fields with a median column density lower than $2 \times 10^{20} \text{ cm}^{-2}$, the PDFs of the residual emission all have skewness and kurtosis values compatible with a Gaussian distribution. Furthermore the width of these PDFs shows very small scatter from field to field (see Fig. 9). This is another indication that, for such diffuse fields, the model is a good description of the data; i.e., the Galactic dust emission is largely dominated by the HI components with very limited spatial variations of the emissivity across a given field.

The dotted line gives the average level of σ_S for these fields with $N_{HI} < 2 \times 10^{20} \text{ cm}^{-2}$. These quantities, together with the average *Planck* or *IRAS* and GBT noise contributions to σ_R , are summarized in Table 1. It is clear from Table 1 and Fig. 9 that even for faint fields σ_S is the main contribution to the rms of the residual, and therefore the main contribution to the dispersion in the dust-gas correlation diagrams in these fields. This is in accordance with the findings of Planck Collaboration (2011n) who concluded that the CIB fluctuations dominate σ_S at 353 GHz and higher frequencies.

At higher column densities, the PDF of the residual shows positive skewness and an rms that increases with N_{HI} , significantly exceeding the level of CIB anisotropies. These aspects of the PDF indicate one or more extra components that contribute to the dust emission and are not taken into account in our model. Contributions to the residual that grow with N_{HI} are compatible with the presence of a molecular gas component. It could also come from spatial variations of the dust emissivity for given HI components or from inadequately-separated HI components.

4.5. Monte-Carlo method to determine emissivity uncertainties

The statistical uncertainties estimated for the emissivities by the least-squares fit method are accurate only for the case of white Gaussian noise in I_v and (sufficiently) low noise in the N_{HI} components. The noise in I_v includes *IRAS* or *Planck* instrumental noise, CIB anisotropies, and various interstellar contaminants, and for the most diffuse fields in our sample, its PDF is close to Gaussian. However, its power spectrum is certainly not white. First, at the angular scales of our observations (from $9'$ to a few degrees), the power spectrum of the CIB anisotropies is $P(k) \propto k^{-1}$ (Planck Collaboration 2011n). Second, the spatial variation of the coverage and the convolution to the GBT resolution both introduce spatial structure in the noise that modifies its power spectrum. The addition of all those noise sources produces a net noise term n_v on I_v that is not white. Because of the random chance correlation of n_v with the N_{HI} components, the uncertainties on the parameters estimated from the least-squares are systematically underestimated (the least-squares fit is not optimal). In addition, the N_{HI} maps are not noise free; significant noise on the independent variable in a least-squares fit produces a systematic bias in the solution. Furthermore, imperfect opacity correction of the HI spectra, the presence of molecular gas, and spatial variations of the dust properties will also produce non-random fluctuations in the residual map. For all of these reasons, an analysis of Monte-Carlo simulations is required for proper estimation of the uncertainties and biases in the ϵ_v^i .

To generate simulations for each field, we adopted the N_{HI} maps obtained from the 21-cm observations as templates of the dust emission. We built dust maps I'_v for each frequency v by adding up these N_{HI} maps multiplied by their respective estimated emissivities ϵ_v^i (just as in computing the residual), to which we added realizations of the *IRAS* or *Planck* noise n_v appropriate to the field⁴ at a level compatible with Table 1 once at GBT resolution, and of the sky residual a_v with a k^{-1} power spectrum at a level to reproduce σ_S within the mask⁵:

$$I'_v = \sum_{i=1}^3 \epsilon_v^i N_{HI}^i + a_v + n_v. \quad (9)$$

Before fitting these simulated data we added white noise to each N_{HI} component at the level estimated for the GBT data (Table A.1). We then carried out the least-squares fit, using the mask already estimated for each field. From a thousand such simulations for each field, we obtained the statistics of the recovered ϵ_v^i so that we could determine if our original fit (fed

⁴ We assumed white noise maps for both *IRAS* and *Planck*, each divided by the square root of their coverage map.

⁵ For the faintest fields this will produce a map with the statistical properties of the CIB anisotropies. For brighter fields, where the residual also includes interstellar contributions, we assumed it also follows a k^{-1} power spectrum but with a greater normalisation (i.e., σ_S) to take into account these effects.

Field	HI	ϵ_{353}	ϵ_{545}	ϵ_{857}	ϵ_{3000}	ϵ_{5000}
AG	Local	-	-	-	-	-
	IVC	0.0246±0.0037	0.0979±0.0123	0.2730±0.0235	0.6100±0.0203	0.1669±0.0092
	HVC	0.0050±0.0025	0.0144±0.0080	0.0280±0.0152	0.0429±0.0145	0.0101±0.0062
BOOTES	Local	0.0450±0.0102	0.1735±0.0300	0.5404±0.0607	0.9471±0.0778	0.2281±0.0301
	IVC	0.0293±0.0069	0.1231±0.0205	0.3729±0.0384	0.8671±0.0497	0.2725±0.0201
	HVC	0.0105±0.0193	0.0366±0.0583	0.0793±0.1072	-0.3957±0.1464	-0.1636±0.0555
DRACO	Local	0.0463±0.0138	0.1878±0.0474	0.5214±0.1070	0.6012±0.1011	0.0867±0.0268
	IVC	0.0477±0.0048	0.1867±0.0152	0.5273±0.0366	0.7335±0.0332	0.1722±0.0093
	HVC	0.0171±0.0069	0.0664±0.0229	0.1516±0.0549	0.1783±0.0476	0.0424±0.0125
G86	Local	0.0337±0.0040	0.1480±0.0122	0.4550±0.0259	0.7125±0.0310	0.1659±0.0084
	IVC	0.0151±0.0019	0.0704±0.0060	0.2387±0.0128	0.6440±0.0148	0.2059±0.0042
	HVC	-0.0539±0.0247	-0.1899±0.0730	-0.3423±0.1561	-0.2199±0.1803	-0.0899±0.0538
MC	Local	0.0306±0.0098	0.1455±0.0313	0.4425±0.0605	0.7745±0.0708	0.1782±0.0287
	IVC	0.0081±0.0090	0.0214±0.0274	0.1579±0.0521	0.6977±0.0594	0.1744±0.0244
	HVC	-0.0052±0.0025	-0.0191±0.0074	-0.0439±0.0147	-0.0292±0.0173	0.0195±0.0073
N1	Local	0.0560±0.0063	0.2149±0.0199	0.5767±0.0362	0.8620±0.0330	0.1662±0.0111
	IVC	0.0387±0.0070	0.1478±0.0222	0.4119±0.0403	0.7232±0.0361	0.2131±0.0117
	HVC	0.0054±0.0044	0.0147±0.0135	0.0353±0.0256	-0.0087±0.0224	-0.0010±0.0074
NEP	Local	0.0453±0.0014	0.1760±0.0051	0.5072±0.0124	0.6942±0.0135	0.1447±0.0047
	IVC	0.0242±0.0013	0.0968±0.0042	0.2781±0.0108	0.6708±0.0122	0.2172±0.0041
	HVC	-0.0096±0.0099	-0.0551±0.0328	-0.1205±0.0849	-0.5746±0.0894	-0.1362±0.0317
POL	Local	0.0506±0.0020	0.1956±0.0081	0.5409±0.0233	0.4405±0.0165	0.1019±0.0040
	IVC	0.0583±0.0124	0.2553±0.0495	0.6625±0.1436	0.7914±0.1006	0.1849±0.0243
	HVC	-	-	-	-	-
POLNOR	Local	0.0540±0.0012	0.2262±0.0045	0.6907±0.0129	0.5887±0.0124	0.0966±0.0027
	IVC	0.0319±0.0083	0.1112±0.0320	0.2684±0.0916	0.5151±0.0806	0.1653±0.0186
	HVC	-	-	-	-	-
SP	Local	0.0632±0.0082	0.2464±0.0255	0.7253±0.0507	0.5877±0.0419	0.0943±0.0166
	IVC	0.0293±0.0076	0.1067±0.0247	0.2935±0.0467	0.7679±0.0399	0.2289±0.0154
	HVC	-0.0032±0.0066	-0.0208±0.0209	-0.0703±0.0408	-0.1158±0.0342	-0.0414±0.0135
SPC	Local	0.0422±0.0013	0.1617±0.0045	0.4528±0.0100	0.4396±0.0084	0.0938±0.0026
	IVC	0.0350±0.0086	0.1322±0.0282	0.3453±0.0681	0.6153±0.0574	0.2249±0.0184
	HVC	0.0049±0.0044	0.0173±0.0144	0.0405±0.0343	0.0076±0.0293	0.0094±0.0089
SPIDER	Local	0.0536±0.0012	0.2254±0.0047	0.6884±0.0130	0.6458±0.0136	0.1078±0.0036
	IVC	0.0271±0.0035	0.0975±0.0134	0.2741±0.0377	0.5637±0.0361	0.2351±0.0103
	HVC	-0.0573±0.0171	-0.1728±0.0653	-0.5330±0.1875	-0.8285±0.1879	-0.2463±0.0512
UMA	Local	0.0529±0.0025	0.2270±0.0107	0.6852±0.0318	0.6143±0.0225	0.1036±0.0045
	IVC	0.0571±0.0060	0.2377±0.0242	0.6967±0.0741	0.7590±0.0520	0.1907±0.0111
	HVC	-0.0173±0.0068	-0.0841±0.0281	-0.2501±0.0852	-0.1844±0.0595	-0.0137±0.0121
UMAEAST	Local	0.0314±0.0027	0.1490±0.0093	0.4848±0.0261	0.5700±0.0163	0.1072±0.0051
	IVC	0.0596±0.0048	0.2223±0.0161	0.5968±0.0458	0.6524±0.0307	0.1913±0.0095
	HVC	0.0059±0.0044	0.0176±0.0161	0.0378±0.0437	0.0400±0.0286	0.0083±0.0086

Table 2. Emissivities of each HI component at 353, 545, 857, 3000, and 5000 GHz. Units are MJy sr⁻¹/10²⁰ cm⁻². The uncertainties were obtained with Monte-Carlo simulations.

into the simulation) was biased and could compare the dispersion of the parameters to the statistical uncertainties returned by the least-squares fitting procedure.

Table B.2 summarizes the results of the Monte-Carlo simulations. Due to random correlation between n_v and the N_{HI} components, we find the Monte-Carlo-derived uncertainty in ϵ_v^i is several times higher than the analytically-derived uncertainty. The results are reported in the table in terms of ϕ_v , the ratio of $\sigma(\epsilon_v^i)$, the standard deviation of the emissivities recovered in the simulations, to $\delta\epsilon_v^i$, the standard deviation expected from the linear fit performed by *Regress*. Therefore, in what follows we use the values of $\sigma(\epsilon_v^i)$ as the uncertainties in ϵ_v^i (see Table 2).

Finally, these simulations make it possible for us to estimate any bias in ϵ_v^i which could arise from the noise in N_{HI} . Table B.2 also provides the bias in %: $b_v = 100(\langle\epsilon_v^i\rangle - \epsilon_v)/\epsilon_v$. Except for some (undetected) HVCs, the bias is only of a few percent; in what follows we made no correction for it.

5. Results

The present study extends to smaller scales, and to the IVCs and HVCs, the earlier work done with the FIRAS (Boulanger et al. 1996) or *IRAS* (Boulanger & Péroult 1988; Reach et al. 1998) data on the dust emission of the diffuse ISM. It also extends to a much larger sample a similar analysis done on a diffuse 3° × 3° region at high Galactic latitude using *IRAS* and *Spitzer* data (Miville-Deschênes et al. 2005). The IR/submm-HI correlation analysis allows us to determine empirically the spectral dependence of the ratio between the dust emission and the gas column density. In addition, the combination of *Planck*, *IRAS*, and N_{HI} data can be used to trace one elusive component of the diffuse interstellar medium: the diffuse H₂ gas (§6.1).

As seen in Figures 7 and 8 there is a clear correlation between the *IRAS* or *Planck* data and N_{HI} in all fields but, as previously seen with *COBE* and *IRAS* data, there are increasing excesses of dust emission with increasing N_{HI} . The estimated emissivities for each field/component/frequency are compiled in

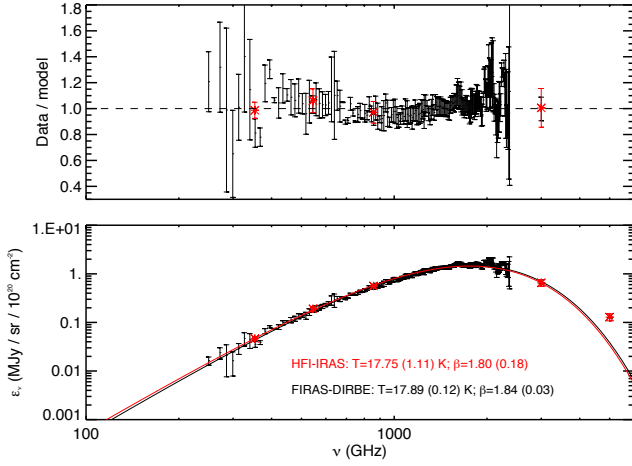


Fig. 10. Bottom panel: Black points show the FIRAS spectrum of the diffuse ISM (Compiegne et al. 2010). The red points are the average of the *IRAS* or *Planck* emissivities for the local components of all our fields; the uncertainty is the variance of the values divided by \sqrt{N} . The solid curves are modified black body fits to each spectrum – the 5000 GHz point was excluded from the fit as it is dominated by non-equilibrium dust emission. **Top panel:** Same as bottom panel but each data set is divided by its modified black body fit.

Table 2. We note that dust associated with the local and IVC components is detected in each field and at each frequency (in AG there is no local gas component). HVC-correlated dust is detected in six of the twelve fields in which there is an HVC gas component (only four detections in both *IRAS* and *Planck*). In this section we analyse what can be drawn from these dust-HI correlation coefficients, the emissivities.

5.1. Comparison with FIRAS data

The FIRAS data provide a reference for the dust emission spectrum of the diffuse ISM. The average FIRAS SED of the high-Galactic latitude sky used by Compiegne et al. (2010) to set the diffuse ISM dust properties in the DUSTEM model is shown in Fig. 10. Also shown in this figure are the current results (red symbols) for the average of the emissivities for the *local* components of our sample at 353, 545, 857, 3000, and 5000 GHz. The *IRAS* and *Planck* data points are found to be fully compatible with the diffuse ISM FIRAS spectrum, showing that our sample is representative of the diffuse dust emission at high Galactic latitudes. We have fit model parameters to both data sets independently using a modified black body function:

$$\epsilon_\nu = I_\nu / N_{HI} = \kappa_0 (\nu / \nu_0)^\beta \mu_{\text{H}} B_\nu(T). \quad (10)$$

where $B_\nu(T)$ is the Planck function and κ_0 is the opacity of the dust-gas mixture at some fiducial frequency ν_0 . (A useful related quantity used below is the emission cross section of the interstellar material per H, $\sigma_e \equiv \mu_{\text{H}} \kappa_0 (\nu / \nu_0)^\beta = \tau / N_{HI}$.) The top panel of Fig. 10 shows the data divided by the model to better display the quality of the fit. The values found for T and β with the two data sets are in close accord. This analysis shows that the local ISM SED can be fit well with $T = 17.9$ K and $\beta = 1.8$.

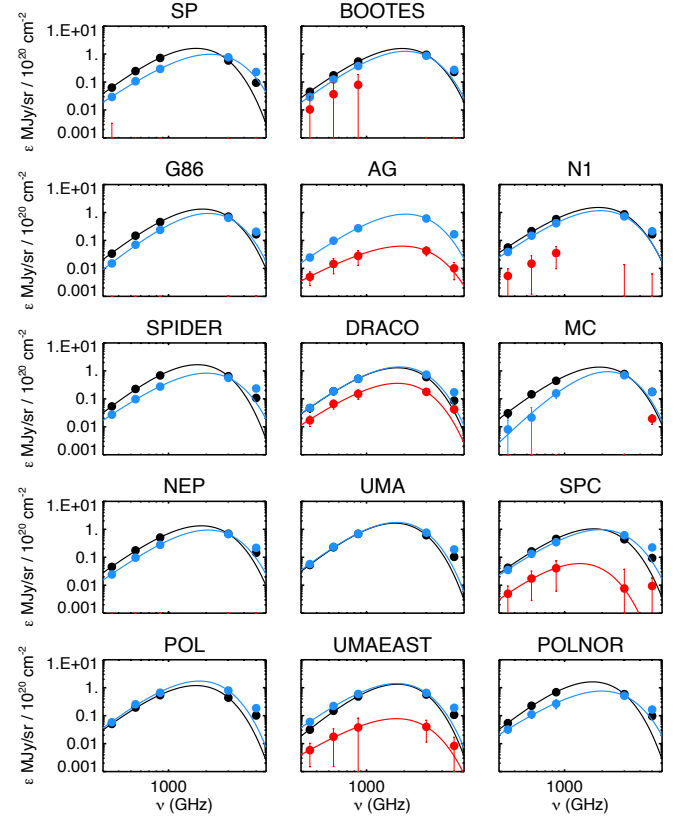


Fig. 11. SEDs from the emissivities of HI components for all the fields in our sample. Black is for the local component, blue for IVC, and red (lowest curves) for HVC. The solid line is a modified black body fit using 353, 545, 857, and 3000 GHz.

5.2. The spectral energy distribution

Fig. 11 shows the dust SED for each field and HI component separately, with the error bars computed using the Monte-Carlo simulations. Like for the FIRAS comparison, each SED was fit using a modified black-body function (solid lines). It has been shown by several studies (Dupac et al. 2003; Désert et al. 2008; Shetty et al. 2009; Veneziani et al. 2010) how difficult it is to estimate separately T and β for such an SED fit. These two parameters are significantly degenerate; their estimate depends greatly on the accuracy of the determination of the error bars on the SED data points. They also depend on the spectral range used to make the fit; for a typical $T = 18$ K dust emission spectrum, the Rayleigh-Jeans range of the black-body curve, where β can be well estimated, corresponds to $\nu < 375$ GHz ($\lambda > 800 \mu\text{m}$).

Despite these caveats, the $T - \beta$ parameter space still provides a way to illustrate the different shapes of the measured SEDs. To make this illustration (and also to compare with previous findings) we present in Fig. 12 the values of T and β found for each HI component, estimated using 353 to 3000 GHz emissivities (The higher-frequency (60 μm) *IRAS* datum is not used in the fit due to contamination by non-equilibrium emission from stochastically-heated smaller grains (Compiegne et al. 2010).) The interesting result from the fits is that the parameters for the local and IVC components lie in significantly different areas of the diagram, because the SEDs are distinctly different. This will be discussed further in the next section. Regarding HVCs, the typical error bars are too large to make any conclusion.

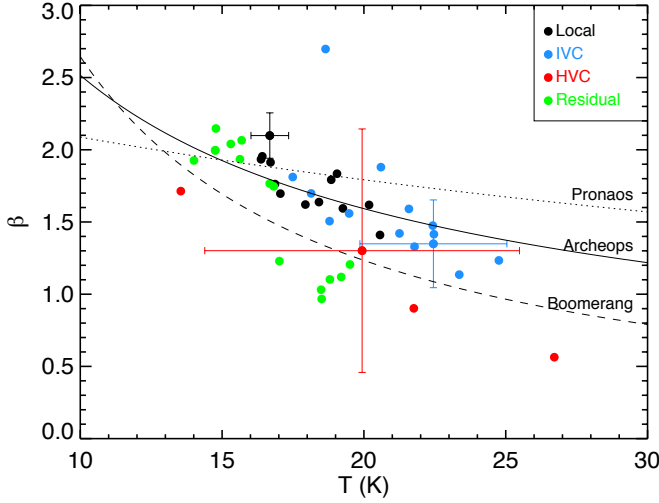


Fig. 12. Parameters of the SED fit: $T - \beta$ diagram. The parameters were obtained using 353, 545, 857, and 3000 GHz data points with uncertainties estimated using the Monte-Carlo analysis. Typical uncertainties on T and β are shown for the three HI components. $T - \beta$ relations obtained with PRONAOS (Dupac et al. 2003), Archeops (Désert et al. 2008) and Boomerang data (Veneziani et al. 2010) are overlaid.

5.3. Dust properties

Because of the above caveats relating to simultaneous fits of T and β , because there are still no firm physical grounds that link T and β according to interstellar dust models, and because the FIRAS spectrum of the diffuse ISM is compatible with $\beta = 1.8$ (in this case the large number of data points and the broad frequency coverage over the peak of the SED give more confidence in the value of β obtained), we have also carried out SED fitting assuming a fixed $\beta = 1.8$. We used a slightly narrower frequency range 545 to 3000 GHz to minimize any effect of β changing with frequency. This provides a direct way to compare not only with the FIRAS spectrum and the DUSTEM model, but also with similar analyses with *Planck* data on molecular clouds and in the Galactic plane (Planck Collaboration 2011o,q,u) that used the same convention. Fixing β has also the advantage of reducing significantly the uncertainty on κ_0 and therefore on the dust emission cross section at a given frequency. In what follows we adopt $\nu_0 = 1200$ GHz to compare directly with the value of $\sigma_e(1200) = (\tau/N_{\text{HI}})_{250\mu\text{m}}$ given by Boulanger et al. (1996).

Fig. 13 shows the values of $\sigma_e(1200)$ estimated assuming a single- T modified black body fit with $\beta = 1.8$ over the range 545 to 3000 GHz. The average for the 13 local components of our sample is $\langle\sigma_e(1200)\rangle = 1.1 \pm 0.3 \times 10^{-25} \text{ cm}^2 \text{ H}^{-1}$, in good agreement with the value of $1 \times 10^{-25} \text{ cm}^2 \text{ H}^{-1}$ obtained by Boulanger et al. (1996). The scatter of $\sigma_e(1200)$ for the local component (30%) is not the result of errors; i.e., there is evidently true variation of the dust properties from one local cloud to another. An alternative explanation would be the presence of different amounts of H_2 gas spatially correlated with the HI. In this case the dust opacity $\sigma_e(1200)$ would be overestimated due to an underestimate of the actual gas column density. Although this scenario cannot be excluded formally, it is not obvious from Fig. 13 where one might expect an increase of $\sigma_e(1200)$ with N_{HI} through the HI- H_2 transition.

The dust opacity is systematically lower for IVCs and HVCs which have $\langle\sigma_e(1200)\rangle = 0.6 \pm 0.4 \times 10^{-25} \text{ cm}^2 \text{ H}^{-1}$ and $\langle\sigma_e(1200)\rangle = 0.17 \pm 0.12 \times 10^{-25} \text{ cm}^2 \text{ H}^{-1}$, respectively. The dust opacity of these clouds also has a significantly greater dispersion than for the local component which implies variations of the dust abundance arising from either dust processing or, for the HVCs, different metallicity.

The dust temperatures obtained with a fixed $\beta = 1.8$ over the range from 545 to 3000 GHz are shown in the middle panel of Fig. 13. The average and standard deviation for the sub-samples of the three HI components – only 4 points for the HVCs – are $T_{\text{local}} = 17.8 \pm 0.9$ K, $T_{\text{IVC}} = 19.6 \pm 1.8$ K, and $T_{\text{HVC}} = 16.4 \pm 2.2$ K. Variations are significant among the fields for each HI component. We note that several IVCs have a temperature significantly higher than what is seen for the local ISM.

The top plot of Fig. 13 shows the energy per H atom E (in W/H) emitted by dust grains (equal to the absorbed energy for grains are at thermal equilibrium) computed by integrating the SED over ν :

$$E = \int 4\pi \kappa_0(\nu/\nu_0)^\beta \mu m_{\text{H}} B_\nu(T) d\nu. \quad (11)$$

Except for the HVCs that have a significantly lower value of E , the striking result here is the small variation of E observed over all the fields and HI components: $\langle E \rangle_{\text{local}} = 3.8 \pm 0.5 \times 10^{-31}$ W/H, $\langle E \rangle_{\text{IVC}} = 3.5 \pm 0.7 \times 10^{-31}$ W/H, and $\langle E \rangle_{\text{HVC}} = 0.5 \pm 0.4 \times 10^{-31}$ W/H. We have checked that the values of E do not depend significantly on fixing β or not. The fact the E is rather constant over all fields and HI components can also be appreciated in Fig. 11 where all SEDs are at about the same level.

The little variations of E is surprising as it implies that the energy absorbed by dust is rather constant, suggesting little variations in the radiation field across all fields, and even in the Galactic halo.

5.4. SED of the residual emission

For all fields the residual emission exhibits significant spatial coherence which reproduces from frequency to frequency (see Figures 2 to 5 and B.2 to B.11). By carrying out a linear correlation analysis between each residual map and the residual map at 857 GHz we estimated the spectrum of this residual emission. The results are presented in Fig. 14. As for the SEDs of the HI-correlated emission, the SEDs of the residual are well fit by a modified black body function.

We note a significant difference in the SED shape between low column density fields and brighter regions. This difference in shape is clearly reflected in the $T - \beta$ diagram (Fig. 12) where green points are for these residual SEDs. The SEDs of brighter fields, where the residual emission is likely to come from molecular gas (§6.1), lie close to $T \sim 15$ K, $\beta \sim 2.0$, a continuation of the locus for the bright HI components. On the other hand, the fainter fields, where the residual emission is most probably dominated by CIB anisotropies, have SEDs well described by $T \sim 19$ K, $\beta \sim 1.2$, well away from the values for any interstellar component in this diagram.

6. Discussion

6.1. The HI- H_2 transition

One possible contribution to the residual emission is dust associated with ionized gas. The WIM has a vertical column density of about $1 \times 10^{20} \text{ cm}^{-2}$ (Reynolds 1989; Gaensler et al. 2008), a

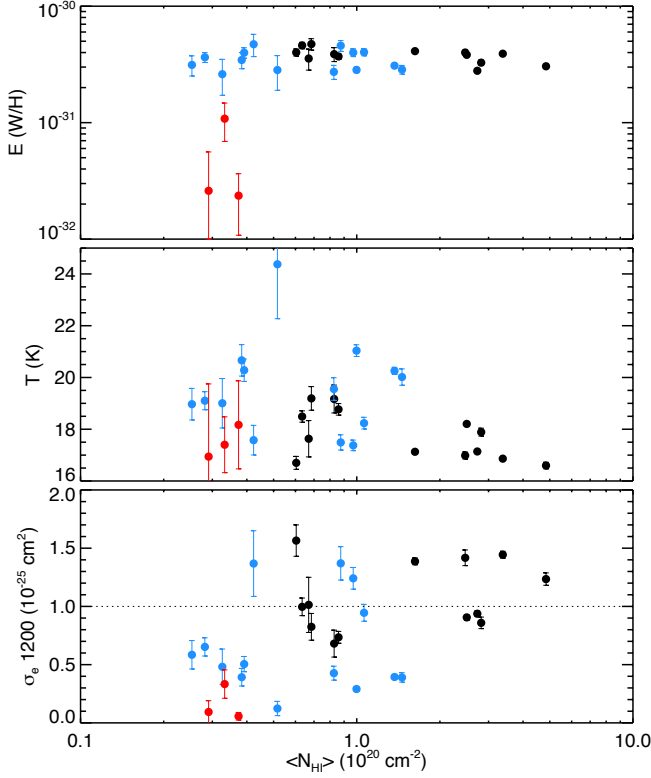


Fig. 13. Bottom panel: $\sigma_e(1200)$, the emission cross section per H at 1200 GHz (250 μm) versus the average column density for the masked points in each field. Black, blue, and red symbols are for local, IVC, and HVC components, respectively. These were estimated from the SED fit over the range 545 to 3000 GHz to a modified black body with $\beta = 1.8$. The dotted line is the global $\sigma_e(1200)$ of the high-latitude diffuse ISM obtained by [Boulanger et al. \(1996\)](#). Middle panel: temperature estimated from the SED fit versus average N_{HI} inside the mask. Top panel: Energy (integral of each SED) versus average N_{HI} inside the mask. Error bars are given for each data point, some being smaller than the symbol size.

significant fraction of the total column density in the most diffuse areas of the sky. [Planck Collaboration \(2011n\)](#) showed that, once the emission correlated with HI is removed from the *Planck* 353, 545 and 857 GHz data in faint fields, the residual emission has a power spectrum compatible with k^{-1} , much flatter than any interstellar emissions. We also showed that the amplitude of the residual in faint fields is constant from field to field (see Fig. 9), compatible with an isotropic extra-galactic emission. These are strong indications that dust emission associated with the WIM, and not correlated with HI, is small.

In fields with bright cirrus, the residuals to the IR-HI correlation are skewed toward positive values, larger than the amplitude of the CIB fluctuations. The most straightforward interpretation is that these positive residuals trace dust emission within H_2 gas. This interpretation is reinforced by the fact that in the brightest fields (e.g., UMA, UMAEAST, and POL) the residual emission is very well correlated with direct measures of the CO emission ([Reach et al. 1998](#)). Therefore, the submm excess emission provides a way to estimate the molecular gas column density, adopting the same emissivity (per hydrogen atom) found for the surrounding HI gas.

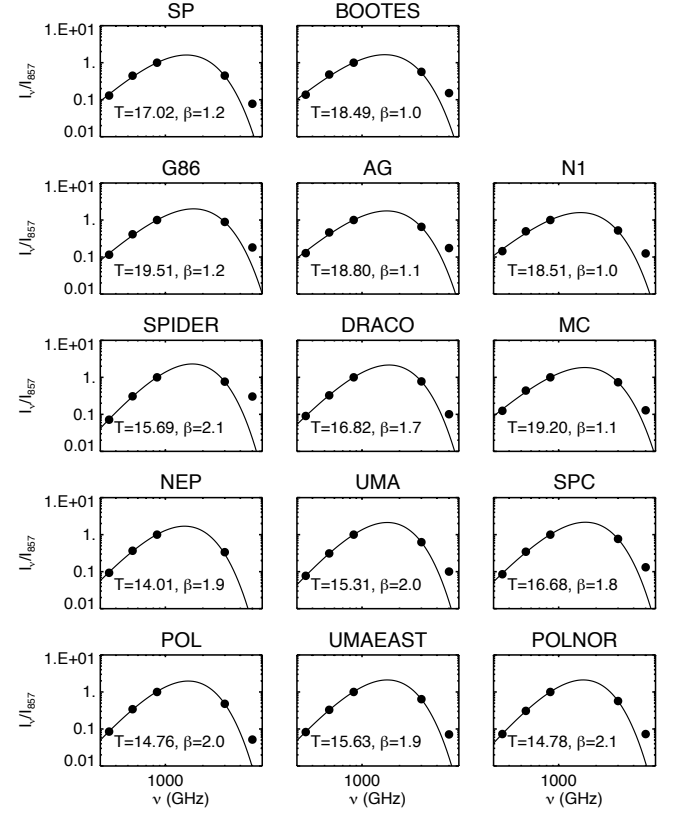


Fig. 14. Correlation coefficient of the residual emission with the 857 GHz residual. Like in Fig. 11 the solid line is the modified black body SED fit done using 3000, 857, 545 and 353 GHz. The values of T and β obtained for each fit are shown.

[Gillmon et al. \(2006\)](#) and [Wakker \(2006\)](#) used Copernicus and FUSE data on H_2 absorption toward extragalactic sources, plus HI emission line observations for the atomic component, to calculate the fraction of mass (or fraction of H nuclei) in molecular form, $f(\text{H}_2) = 2N_{\text{H}_2}/(2N_{\text{H}_2} + N_{\text{HI}})$, on these lines of sight. They plotted $f(\text{H}_2)$ versus $N_{\text{H}}^{\text{tot}}$ (the denominator in the above fraction). We produce a similar plot in Fig. 15 using the data from [Gillmon et al. 2006](#). The plot shows a transition from low to high $f(\text{H}_2)$ beginning at a column density $N_{\text{H}}^{\text{tot}} \sim 3 \times 10^{20} \text{ cm}^{-2}$. However, these lines of sight do not probe column densities as high as found in some parts of our survey. Comparable column densities are probed toward O stars near the Galactic plane ([Rachford et al. 2009](#)), also shown in the figure. These show a scatter of $f(\text{H}_2)$ reaching the level we find (see below).

[Wakker \(2006\)](#) found only very low amounts of molecular hydrogen in IVC and HVC gas, and so the transition is occurring in the local ISM. He emphasized that it is not straightforward to relate this transition to physical properties of the interstellar gas, like density in the molecule-producing environment, or even a physical threshold in column density required for molecule formation, because of the summing over different environments along the line of sight. A corollary is that there can be quite different values of $f(\text{H}_2)$ for the same $N_{\text{H}}^{\text{tot}}$, as is seen in the figure.

There is a possibility that the pencil-beam UV absorption measurements could have missed the bulk of the H_2 gas, depending on the covering factor of a potentially clumpy molecule-

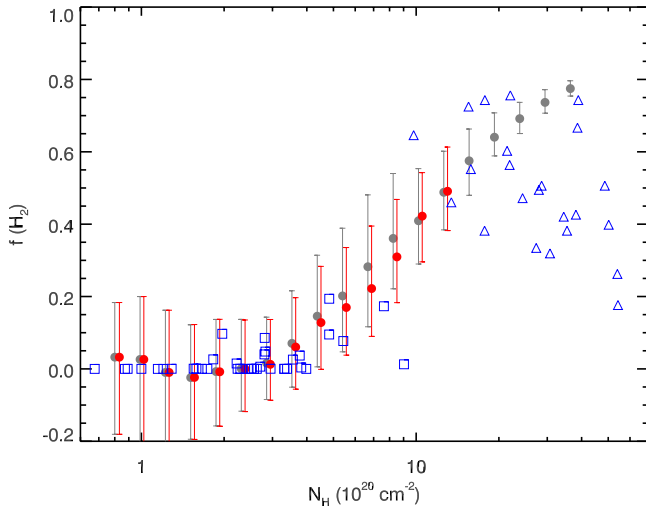


Fig. 15. Fraction $f(\text{H}_2)$ of hydrogen that is in molecular form in local gas, calculated from emission excess relative to the linear correlation (see text), versus the total column density. At low column density, the sensitivity to detect molecular hydrogen is low because of the CIB fluctuations, but at higher column densities the molecular fraction is large enough to be detected. Red points are for lines of sight with no detectable CO emission, whereas black points include all lines of sight. We see that there are lines of sight with no CO where we still infer molecular hydrogen, the so-called “dark gas.” This molecular gas can be detected by UV absorption. Data from high-latitude surveys (Gillmon et al. 2006; Wakker 2006, squares) show the same column density threshold for molecular hydrogen to be seen at the few percent level but the UV survey lines of sight do not intercept the higher column densities reached in some parts of our surveys. Comparable column densities are reached toward O stars on lines of sight closer to the Galactic plane (Rachford et al. 2002; Rachford et al. 2009, triangles), but these do not uniformly show as high a molecular fraction as we find.

containing environment, and so comparison with the complementary infrared/submm analysis is of great interest.

We carried out our analysis beginning with the I_{857} dust maps. To concentrate on the local gas, we removed the IVC and HVC-correlated emission, and the constant term, using the results of the linear regression in each field. This left a map of local emission, as used to make the plots in the left column of Figs. 7 and 8. Dividing this by ϵ_{local} for each field produces a map of the total column density $N_{\text{H}}^{\text{tot}}$ for the local gas, assuming the emissivity is the same in the molecular gas as in the atomic gas from which it formed. We of course have a map of the local atomic column density ($N_{\text{HI}}^{\text{local}}$) from the GBT measurements. Therefore, we are able to compute the molecular column density map $N_{\text{H}_2} = (N_{\text{H}}^{\text{tot}} - N_{\text{HI}}^{\text{local}})/2$ and then $f(\text{H}_2)$ pixel by pixel.

Combining all fields⁶ we binned the data in $N_{\text{H}}^{\text{tot}}$ and within each bin examined the PDF of $f(\text{H}_2)$, finding its median and half-power points (which are not necessarily symmetrical). The results plotted in Fig. 15 reveal an increase in $f(\text{H}_2)$ beginning at $N_{\text{H}}^{\text{tot}} \sim 3 \times 10^{20} \text{ cm}^{-2}$, the same as in the direct UV analysis. Note that we are not sensitive to the much lower values of $f(\text{H}_2)$ found

at low column densities, because of the contaminating CIB fluctuations.

At intermediate column densities, even for lines of sight with no CO (red circles - see Planck Collaboration (2011o)), we see a rise in $f(\text{H}_2)$, and the lines of sight with CO extend this rise further at higher column densities. This supports our interpretation of the excess being caused by dust associated with molecular hydrogen. We call this medium “dark gas” if it is not detected via CO (Planck Collaboration 2011o).

Note that the UV observations toward O stars give some $f(\text{H}_2)$ values at the same level as we find, but also some much lower values for a given column density. This suggests that the UV observations are somewhat affected by clumpiness and/or are sampling qualitatively different lines of sight than ours at high latitude.

Although there are lines of sight where $f(\text{H}_2)$ is quite high, summed over all lines of sight in our survey, our study shows that the excess emission at 857 GHz that is not correlated with HI is only 10% of the total emission. Thus the fraction of the hydrogen gas mass that is in molecular form in this sample of the high latitude diffuse interstellar medium in the solar neighborhood is quite low. Planck Collaboration (2011o) estimated 35% for the entire high-latitude sky above 15° , which includes higher column density lines of sight. Of this 35%, about half is traced by CO, leaving about 20% as “dark gas” not traced by CO or HI.

The structure and nature of the diffuse molecular gas can be studied using the maps of residual (excess) dust emission. In SPIDER (see Fig. 5), an intermediate column density field where there is very little CO emission detected (Barriault et al. 2010), we observe coherent filamentary structures in the residual map that we interpret as the presence of dust in diffuse H_2 gas without CO. We have checked that the structures could not be accounted for by an underestimate of the 21-cm line opacity correction, even with T_{spin} as low as 40 K. In this case the submm residual provides a way to map directly the first steps of the formation of molecules in the diffuse ISM.

6.2. Evolution of dust

6.2.1. Variations of the big grain emission cross section

Interstellar dust evolves through grain-grain and gas-grain interactions. Fragmentation and coagulation of dust grains are expected to occur in the ISM, modifying not only the grain size distribution but also the grain structure. The data described here provide important evidence for dust processing in diffuse local clouds and IVCs. As we will elucidate, the evidence can be seen in Figures 16 and 17.

Fig. 16 shows the values of T versus $\sigma_e(1200)$ (see Fig. 13) for each HI component together with the values found in the Taurus molecular cloud (Planck Collaboration 2011u) averaged in bins of $\sigma_e(1200)$ (green points). The solid line shows the expected values of T and $\sigma_e(1200)$ for a constant emitted energy E (normalized to the average diffuse ISM values: $T = 17.9 \text{ K}$ and $\sigma_e(1200) = 1.0 \times 10^{-25} \text{ cm}^2$).

The cross section σ_e reflects the efficiency of thermal dust emission per unit mass. Dust that emits more efficiently will have a lower equilibrium temperature, the trend seen. Note that the dust in very different environments has close to the same integrated emission and therefore is absorbing about the same energy (solid line). The comparison with the Taurus molecular cloud data suggests that the $T - \sigma_e$ anti-correlation extends to colder dust (we note that the Taurus data points are slightly

⁶ except AG because there is no local component and DRACO because its excess emission is likely to be dominated by Intermediate-Velocity gas (Herbstmeier et al. 1993)

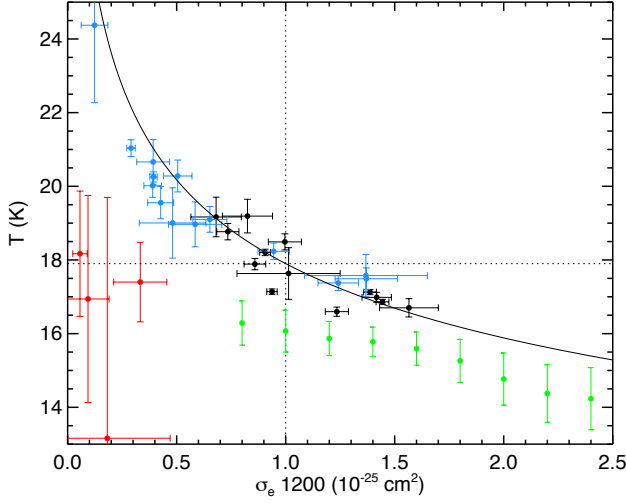


Fig. 16. Temperature vs emission cross section estimated from 545 to 3000 GHz with $\beta = 1.8$. Black is local, blue is IVCs, red is HVCs and green is the data points obtained on the Taurus molecular clouds (Planck Collaboration 2011u). For the latter the error bars give the dispersion of T in each bin of σ_e . The solid line represents a constant emitted energy for the diffuse ISM reference values ($\sigma_e = 1 \times 10^{-25} \text{ cm}^{-2}$ and $T = 17.9 \text{ K}$ - dotted lines).

shifted corresponding to a lower E , in accordance with a lower radiation field strength than in the diffuse ISM, possibly due to extinction).

Fig. 17 complements Fig. 16 by comparing directly measured emissivities (ϵ_ν) with the DUSTEM model of the diffuse ISM. This comparison, independent of any grey body fit, also shows strong evidence for dust evolution. The top plot of Fig. 17 shows the 857 GHz emissivity (or emission per N_H) versus the 3000 GHz to 857 GHz ratio which increases steadily with the dust temperature T . The DUSTEM model (lines) predicts an increase of ϵ_{857} with $\epsilon_{3000}/\epsilon_{857}$, the opposite of the trend observed. The assumption used to produce the DUSTEM curve is that grain optical properties are constant and that the variations in ϵ_{857} and $\epsilon_{3000}/\epsilon_{857}$ are solely due to variations in the radiation field (from $G = 0.1$ to $G = 5$ in this diagram). Again the data points do not favor this trend but are consistent with a decrease of the dust emission cross section ($\sim \epsilon_{857}$) with temperature ($\sim \epsilon_{3000}/\epsilon_{857}$), the same trend seen in Fig. 16.

An evolutionary model in which dust structure changes due to aggregation (and the reverse process, fragmentation) is qualitatively consistent with these results: grains with a fluffy structure will absorb about the same amount of optical and ultraviolet radiation per unit mass as more compact grains, but compared to these more homogeneous and spherical grains they are more emissive at submm wavelengths because of their more complex structure (Stepnik et al. 2003).

6.2.2. Dust shattering in Intermediate Velocity clouds?

The bottom plot of Fig. 17 shows the 5000 GHz to 857 GHz emissivity ratio as a function of the 3000 GHz to 857 GHz ratio for all H I components and the residual emission. The locus from standard ISM DUSTEM models shows an effect of increasing colours with increasing G . The local component of bright cirrus clouds (black crosses at the left end of the plot) and the green

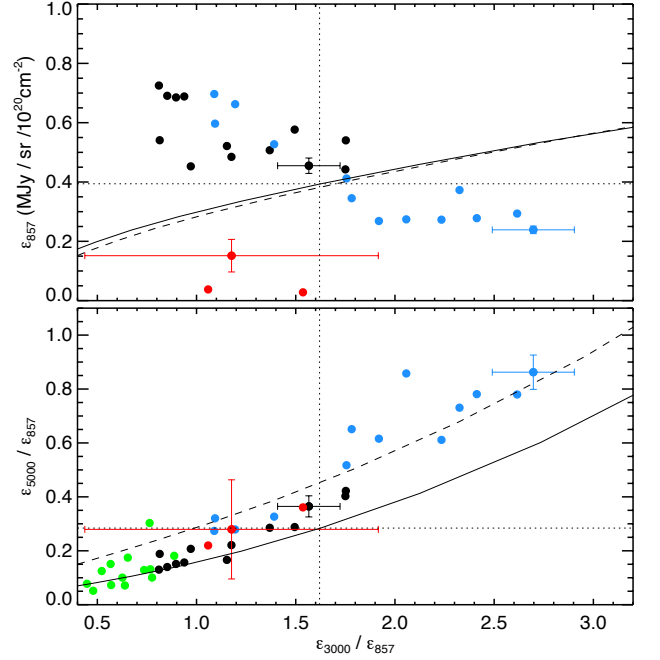


Fig. 17. Bottom : 5000/857 GHz (60/350 μm) ratio as a function of the 3000/857 GHz (100/350 μm) ratio. Top : dust emission per N_{HI} at 857 GHz versus the 5000/857 GHz ratio. Local (black), IVC (blue), HVC (red), residual (green). Solid line is the DUSTEM model for the diffuse ISM, with radiation field variations from $G = 0.1$ to $G = 5$. Dashed line is the same model but with a relative abundance of VSGs four times higher than the standard diffuse ISM value. Dotted lines give the local ISM fiducial values ($G = 1.0$). Typical uncertainties are shown for each H I component.

stars from molecular residuals have colours in good agreement with the standard DUSTEM model.

Both ratios are higher for the IVCs and the trend is offset relative to the standard locus. The qualitative interpretation is that the emission in these higher-frequency bands is more contaminated by non-equilibrium emission from an increased relative abundance of very small grains (VSGs) compared to the larger grains (BGs) in thermal equilibrium. To make this more quantitative, the dashed curve passing closer to the IVC data shows the colours for a DUSTEM diffuse ISM model with a relative abundance of VSGs four times higher than the standard value.

Note that because of their non-equilibrium emission, VSGs dominate the emission for $\nu > 5000 \text{ GHz}$ and seriously contaminate the *IRAS* 60 μm band in the standard DUSTEM model even with an abundance of only 1.6% of the total dust mass. The VSGs are carbonaceous grains in the DUSTEM model (the SamC component). By contrast, the BGs make up 90.7% of the total dust mass, 14.2% carbon rich and 76.5% silicates. Recall that for the IVCs the dust opacity $\sigma_e(1200)$ for the BGs is about a factor of two lower than for the local ISM, which can be interpreted as simply a factor of two reduction in the mass of BGs. Thus the four-times higher relative abundance of VSGs to BGs corresponds to only about a factor of two net abundance increase of the VSGs in the IVCs. This is easy to accommodate by shattering of a small fraction of the BG dust mass. It might be that the composition of VSGs changes dramatically, from carbon rich to silicates, given the relative mass available in BGs. The details

would be linked to the specific dynamical and shock history of this interstellar matter that is part of the Galactic fountain.

Observed variations in the level of depletion of atoms with gas velocity and from CNM to WNM lines of sights (Jenkins 2009) suggest there is lower depletion in IVCs. Depending on the element, some with very high depletion, gas phase abundances can be very sensitive to the return of even small fractions of the element to the interstellar gas. Furthermore, while the reduction of depletion indicates the evolution of dust, it is difficult to distinguish between dust erosion and dust destruction.

6.3. Dust in high-velocity clouds

Dust emission correlated with HVC gas continues to be difficult to establish because of the contaminating foreground emission of local and IVC components and the background CIB fluctuations which greatly increase the uncertainties in ϵ_v^{HVC} (§4.5 and Table B.2). Furthermore, the dust fraction must be intrinsically low due to the low metallicity (Collins et al. 2007). Some fields, of course, just have little HVC gas (Table A.1).

At first glance, examination of the SEDs in Fig. 11 shows encouraging evidence for an HVC detection in some fields, like AG. However, the apparent systematic behaviour across the SED does not necessarily bolster the statistical significance of the detection in a single pass band. This is because the dust emission is intrinsically highly correlated frequency to frequency, as is the CIB, and so given the generally small noise, the fits to the correlations with (the same) N_{HI} are to first order just scaled versions of each other.

At best, the HVC-correlated emission is detected only marginally, at a level ranging from 1.2σ to 3.75σ (Table 2). The only potential detection at the $3\text{-}\sigma$ level is in the DRACO field, not because the uncertainty is particularly low but because the emissivity seems unusually high for an HVC. The metallicity in “complex C” (the large HVC complex sampled in part by the Draco field) does reach 0.3 solar, possibly by mixing with halo gas (Collins et al. 2007). The low values of $\sigma_e(1200)$ indicate a lower dust-to-gas mass ratio than in the local and IVC gas, in agreement with a smaller HVC metallicity (Collins et al. 2007) and with previous work (Miville-Deschênes et al. 2005).

7. Conclusions

We have presented results of a first comparison of *Planck* and *IRAS* with new HI 21-cm line GBT data for 14 high Galactic latitudes fields, covering about 825 square degrees on the sky. Using the velocity information of the 21-cm data we made column density maps of the local ISM, IVC, and HVC in each field. By correlating these HI maps with the submm/infrared dust emission maps we estimated the distinct dust emissivities for these three high-latitude components and made corresponding SEDs from 353 to 5000 GHz.

The average SED of the local ISM dust deduced from the *IRAS* and *Planck* data is compatible with that from the FIRAS data over the high-latitude sky and is well fit with a modified black body with parameters $\beta = 1.8$ and $T = 17.9$ K. On the other hand, even though the energy emitted by dust is rather constant in our sample, we report significant variations of the dust SED shape, compatible with variations of the dust temperature anti-correlated with the emission cross section. We interpret these variations as a signature of active evolution of the dust grain structure through coagulation and fragmentation in the diffuse ISM.

For faint cirrus fields with average HI column density lower than $2 \times 10^{20} \text{ cm}^{-2}$, the residual FIR-submm emission, after removal of the HI-correlated contributions, is normally distributed with a standard deviation compatible with the expected level of CIB fluctuations. The SED of the residual is unlike any interstellar component. For such diffuse fields we also show that the interstellar dust emission is dominated by the contribution from atomic gas.

For fields with larger HI column density there are significant FIR-submm emission excesses that, for the brightest fields, follow the structure of the CO emission. For intermediate column density regions, the residual emission shows coherent spatial structures not seen in CO, revealing the presence of H_2 gas. The SED of this residual shows that it is slightly colder than the dust in the local HI. There is a lot of variation in $f(H_2)$, the fractional mass in the form of H_2 , but over the whole survey of these diffuse fields the fraction is only 10%.

We report strong detection of dust emission from all IVCs in our sample. The dust emission cross section is typically two times lower than for the local ISM and the relative abundance of small grains having non-equilibrium emission is about four times higher than normal. This evolution of the dust properties is indicative of dust shattering in halo gas with the dynamics of a Galactic fountain. We also find that, compared to the local ISM, several of these clouds have a higher dust temperature which could also be the result of globally smaller grains. The total energy emitted by dust in IVCs is comparable to what is observed in the local ISM suggesting similar radiation field strength.

Finally we report on attempts to detect HVC-correlated dust emission. We show that this is very challenging given the uncertainties induced by the CIB anisotropies and the expectation of lower emissivity because of the low metallicity. There is only one field with a detection near the 3σ level. The low limits on emissivity and dust opacity, 3–10 times smaller than the values in the local ISM, are indeed in accordance with the low metallicity in HVC clouds. The temperature (or range of temperatures) for this potential HVC-related dust is difficult to establish because of the low signal-to-noise ratio.

Acknowledgements. A description of the Planck Collaboration and a list of its members can be found at http://www.rssd.esa.int/index.php?project=PLANCK&page=Planck_Collaboration

Appendix A: Noise of the HI components

The analysis presented here relies on a correlation between far-infrared/submm data and the HI components deduced from 21-cm emission. In order to estimate properly the uncertainties on the correlation coefficients the noise on the HI components needs to be evaluated. We have made this estimate using two different methods which address different contributions to the noise (see Boothroyd et al. (2011)).

First we applied the traditional method in which the end channels of the 21-cm spectrum, where there is no emission. The velocity channels are independent, i.e., the spectrometer resolution is better than the 0.8 km s^{-1} channel width. A large number of end channels can be used to compute a map of the standard deviation of the noise at each (x, y) position:

$$\delta_{Tb}(x, y) = \sqrt{\frac{1}{N_\delta - 1} \sum_{v=v_1}^{v_2} T_b^2(x, y, v) - \frac{1}{N_\delta} \left(\sum_{v=v_1}^{v_2} T_b(x, y, v) \right)^2} \quad (\text{A.1})$$

where $N_\delta = v_2 - v_1 + 1$ is of the order of 200 channels. For the GBT data, this is a very flat map, whose typical value is the same as the standard deviation of a single end channel. This is about 0.17 K for a single visit to a field. Some fields were mapped two or three times.

The uncertainty map $\delta N_{HI}(x, y)$ for the column density of a given HI component summed over N channels is

$$\delta N_{HI}(x, y) [\text{cm}^{-2}] = A \sqrt{N} \delta_{Tb}(x, y) \Delta v, \quad (\text{A.2})$$

Field	l (deg)	b (deg)	Area (deg ²)	$\langle N_{HI}^{local} \rangle$ (10^{20} cm^{-2})	δN_{HI}^{local} (10^{20} cm^{-2})	$\langle N_{HI}^{IVC} \rangle$ (10^{20} cm^{-2})	δN_{HI}^{IVC} (10^{20} cm^{-2})	$\langle N_{HI}^{HVC} \rangle$ (10^{20} cm^{-2})	δN_{HI}^{HVC} (10^{20} cm^{-2})
AG	164.8	65.5	26.4	0.0000	0.0000	1.4758	0.0426	0.3754	0.0253
BOOTES	58.0	68.6	49.1	0.6928	0.0122	0.3937	0.0149	0.0170	0.0152
DRACO	92.3	38.5	26.4	0.6792	0.0124	1.1490	0.0197	0.3436	0.0337
G86	88.0	59.1	26.4	0.8805	0.0131	1.0252	0.0170	0.0360	0.0150
MC	56.6	-81.5	30.7	0.8422	0.0205	0.5216	0.0133	0.6167	0.0350
N1	85.3	44.3	26.4	0.6402	0.0235	0.2836	0.0193	0.2965	0.0257
NEP	96.4	30.0	146.5	2.6163	0.0193	1.4413	0.0179	0.1105	0.0161
POL	124.9	27.5	60.6	6.2571	0.0512	0.4954	0.0289	0.0000	0.0000
POLNOR	125.0	37.4	60.6	3.9444	0.0370	0.3371	0.0213	0.0000	0.0000
SP	132.3	47.5	26.4	0.6079	0.0206	0.3847	0.0213	0.1786	0.0212
SPC	135.6	29.3	102.1	3.0267	0.0383	0.2676	0.0199	0.0896	0.0222
SPIDER	134.9	40.0	103.8	1.8541	0.0197	0.8353	0.0290	0.0269	0.0183
UMA	144.2	38.5	80.7	2.7976	0.0309	0.9051	0.0310	0.0989	0.0283
UMAEAST	155.7	37.0	61.3	3.1700	0.0320	0.9514	0.0298	0.2858	0.0393

Table A.1. Average column density and uncertainties for each HI component of each field. No local component could be identified for field AG. Likewise, no HVC component is present in the POL and POLNOR fields.

where Δv is the channel width in km s^{-1} . For $N \sim 60$, this amounts to $\delta N_{HI} \sim 0.02 \times 10^{20} \text{ cm}^{-2}$ for a single visit. This assumes, as is usual, that the noise properties estimated using the end channels are representative of the noise in channels summed to build the column density maps. Actually, the channel noise scales as roughly $(1 + T_b/20\text{K})$ and this can be taken into account.

We developed a second method which exploits the fact that the HI brightness-temperature cubes were built by averaging independent data taken in different polarisations (called XX and YY). Each polarisation observation can be reduced separately, which requires separate baseline estimates for the spectra in the XX and YY cubes. Baseline fitting is another source of error. Taking the difference between the XX and YY cubes removes the common unpolarized H I emission, leaving in each velocity channel only the thermal noise and systematic effects from the baseline subtraction. The difference cube is

$$\Delta(x, y, v) = (T_{XX}(x, y, v) - T_{YY}(x, y, v))/2, \quad (\text{A.3})$$

where we divide by two to give the same statistics as in the average of the cubes.

We make a map of the column density differences (divided by two) over the same channel range as for N_{HI} :

$$\Delta N_{HI}(x, y) = A \Delta v \sum_{v=v1}^{v2} \Delta(x, y, v). \quad (\text{A.4})$$

The estimate of δN_{HI} is then the standard deviation of this map.

This method gives an uncertainty typically 1.3 times the simple estimate using end channels (it can reach up to 2 times for the brightest components) because it includes baseline uncertainties and the increase of thermal noise with signal. The column density uncertainties evaluated with this second method for each component in each field are given in Table A.1). There are additional errors from the stray radiation correction that can affect the local and IVC components. The total uncertainty including this additional contribution can be estimated in a similar way to the second method if there are two or more visits to compare (Boothroyd et al. 2011). Because in cases with multiple visits these are found to be not much larger, and because the uncertainties in N_{HI} are not the major source of uncertainty in the correlation analysis (§4.5), adopting the values in Table A.1 is satisfactory for our purposes.

Appendix B: Estimating the noise of the *Planck* and *IRAS* maps

To estimate the noise level of the *IRAS* and *Planck* maps we use the difference between independent observations of the same sky. For *IRAS*, the original ISSA plates (Wheelock et al. 1993) were delivered with three independent set of observations (called HCONs), each obtained at different periods during the life of the satellite. Each HCON has its own coverage map. The ISSA final product is the coverage-weighted co-addition of the three HCONs. The IRIS product (Miville-Deschênes & Lagache 2005) also contains the three HCONs.

For *Planck*, we also have access to independent observations of the same sky. For each pointing period *Planck* scans the sky about 50 times. The Data Processing Centre delivered two maps made with data from the first half and second half of each pointing period, respectively. In this case the number of samples used to estimate the signal at a given sky position is the same in the two maps

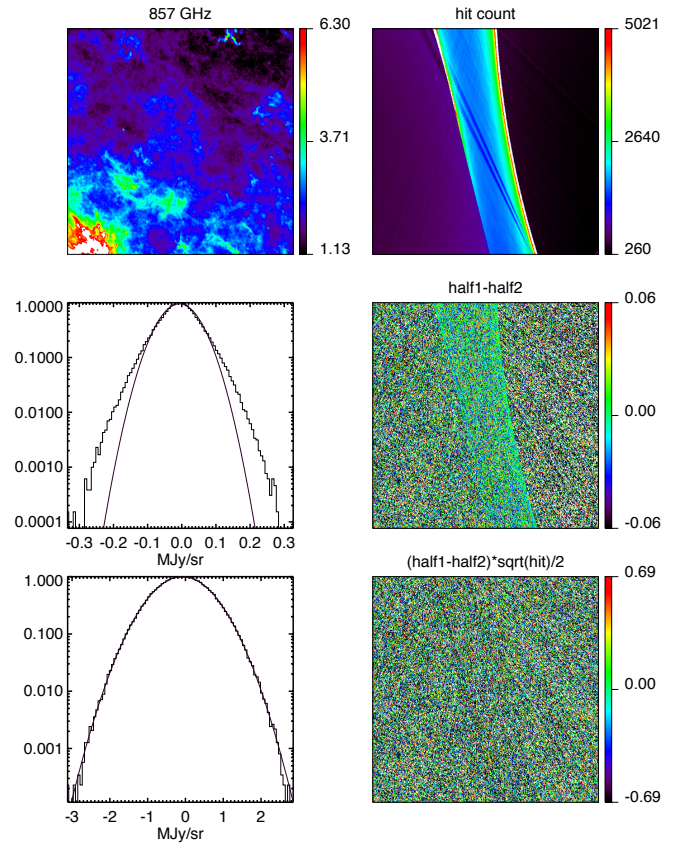


Fig. B.1. Noise and coverage of the 857-GHz *Planck* map of the NEP field. Top row : 857 *Planck* map in MJy sr^{-1} and coverage map. Middle row : Difference map and its PDF (with Gaussian fit). Bottom row : difference map de-weighted by the coverage and its PDF (with Gaussian fit).

(i.e., the coverage map is identical for the two maps). Fig. B.1 shows the three *Planck* maps used for the NEP field, the difference maps, and the coverage maps, and the difference maps properly weighted by the square root of the coverage. From the latter, one can appreciate the homogeneity and Gaussian distribution of the *Planck* noise.

Field	σ_{noise}^{353}	σ_{noise}^{545}	σ_{noise}^{857}	σ_{noise}^{3000}	σ_{noise}^{5000}
AG	0.0055	0.0095	0.0094	0.0295	0.0156
BOOTES	0.0078	0.0122	0.0124	0.0243	0.0156
DRACO	0.0044	0.0075	0.0073	0.0234	0.0115
G86	0.0056	0.0085	0.0086	0.0243	0.0147
MC	0.0088	0.0140	0.0139	0.0306	0.0172
N1	0.0050	0.0084	0.0083	0.0218	0.0120
NEP	0.0040	0.0065	0.0063	0.0265	0.0138
POL	0.0061	0.0095	0.0098	0.0333	0.0141
POLNOR	0.0054	0.0087	0.0088	0.0252	0.0134
SP	0.0055	0.0086	0.0088	0.0268	0.0153
SPC	0.0065	0.0104	0.0104	0.0280	0.0142
SPIDER	0.0058	0.0093	0.0096	0.0277	0.0143
UMA	0.0065	0.0101	0.0108	0.0340	0.0156
UMAEAST	0.0072	0.0111	0.0113	0.0365	0.0167

Table B.1. *Planck* and *IRAS* noise levels (in MJy sr⁻¹) for each field and at each frequency. The value given here is the noise level in the map that has been convolved to the 9.4' GBT resolution.

Here we want to estimate the average noise level δI_ν of an *IRAS* or *Planck* map I_ν used for the analysis, given its coverage map N_ν and a difference map

$$\Delta_\nu(x, y) = (I_\nu^1(x, y) - I_\nu^2(x, y))/2 \quad (\text{B.1})$$

obtained from independent observations, each I_ν^i map having its own coverage map N_ν^i . In the general case (Miville-Deschênes & Lagache 2005), δI_ν is obtained by taking the standard deviation of the map

$$\Delta'_\nu(x, y) = \Delta_\nu(x, y) \sqrt{\frac{4N_1(x, y)N_2(x, y)}{N(x, y)(N_1(x, y) + N_2(x, y))}}. \quad (\text{B.2})$$

In the case of *Planck*, $N_1 = N_2 = N/2$ and so $\Delta'_\nu = \Delta_\nu$ and the standard deviation of the average map is the same for the difference map, as expected. Because the ISSA plates are the combination of three observations with different coverages such a simplification is not possible and the above more general equation has to be used.

In our analysis we used the *IRAS* and *Planck* maps convolved to the 9.4' resolution of the GBT. Therefore, the appropriate δI_ν is obtained by first convolving the $\Delta'_\nu(x, y)$ map and then taking the standard deviation. These are the noise levels tabulated for each field in Table B.1.

Field	HI	δ_{353}	δ_{545}	δ_{857}	δ_{3000}	δ_{5000}	ϕ_{353}	ϕ_{545}	ϕ_{857}	ϕ_{3000}	ϕ_{5000}	b_{353}	b_{545}	b_{857}	b_{3000}	b_{5000}
AG	Local	1.00	1.01	1.02	1.00	1.05	8.13	8.73	8.71	7.41	8.09	-1.82	-1.24	-1.63	-1.84	-1.80
	IVC	1.00	1.01	1.03	1.01	1.06	8.05	8.31	8.24	7.41	7.91	0.17	2.41	1.31	2.12	0.76
	HVC	1.00	1.01	1.03	0.96	0.92	10.65	11.38	12.87	11.35	10.43	-1.65	-1.44	-1.42	-1.81	-1.71
BOOTES	Local	1.01	1.02	1.04	0.97	0.93	12.44	13.47	14.03	12.53	12.04	-0.83	-0.64	-0.82	-1.23	-0.83
	IVC	0.83	0.84	0.86	0.79	0.76	4.08	4.49	4.61	4.33	3.90	-37.40	-24.59	-29.53	-35.32	-34.58
	HVC	1.11	1.13	1.26	1.15	1.06	8.71	9.23	9.86	9.27	8.22	-1.56	-1.79	-1.54	-1.71	-1.26
DRACO	Local	1.07	1.09	1.21	1.11	1.02	8.93	8.80	10.02	9.03	8.42	-0.60	-0.06	-0.58	-0.14	-0.35
	IVC	1.05	1.06	1.18	1.09	1.00	6.84	7.02	7.97	6.87	6.05	-3.43	-2.85	-2.14	-3.22	-1.20
	HVC	0.99	0.99	0.99	0.96	1.00	8.67	8.96	8.97	8.68	8.20	1.06	1.02	0.48	0.20	-0.09
G86	Local	1.00	1.00	1.00	0.97	1.01	7.61	8.24	8.33	7.79	7.69	0.37	0.64	-0.18	-0.01	-0.08
	IVC	0.92	0.92	0.92	0.90	0.93	5.51	5.52	5.59	5.22	5.45	-12.72	-14.42	-13.06	-16.41	-16.79
	HVC	0.98	0.98	0.98	0.99	0.98	7.69	9.11	9.45	9.00	8.57	-4.64	-2.39	-2.98	-2.74	-3.36
MC	Local	0.98	0.98	0.99	1.00	0.99	6.28	7.06	7.22	6.70	6.46	0.58	-4.90	-0.29	-1.77	-2.60
	IVC	0.99	0.99	1.00	1.01	1.00	7.01	7.52	7.99	7.66	7.59	-2.76	0.74	-2.03	-0.82	-1.10
	HVC	0.99	0.99	0.99	1.00	1.02	7.63	8.23	8.08	7.52	7.28	-1.74	-1.31	-1.24	-1.45	-1.64
N1	Local	0.99	0.99	1.00	1.00	1.03	7.83	8.22	8.40	7.65	7.51	-0.41	-9.13	-9.12	34.57	66.38
	IVC	0.99	0.99	1.00	0.92	0.76	10.54	10.97	11.01	9.73	7.85	-0.18	-0.05	-0.19	-0.30	-0.65
	HVC	0.99	0.99	1.00	0.92	0.76	12.70	12.42	13.26	12.13	9.60	-0.23	-0.18	-0.23	-0.06	-0.10
NEP	Local	0.99	0.99	1.00	0.92	0.76	10.36	10.36	11.10	9.47	7.82	-9.24	-3.75	-6.32	-3.34	-4.75
	IVC	0.98	0.98	0.99	0.91	0.75	6.58	8.21	9.52	6.29	5.63	-0.10	-0.03	0.01	0.06	0.07
	HVC	0.93	1.08	1.26	0.87	0.79	6.07	7.38	8.59	5.60	5.00	-2.32	-2.55	-1.86	-2.46	-2.34
POLNOR	Local	1.01	1.03	1.03	1.00	1.02	10.09	10.41	10.53	10.58	10.51	-0.04	-0.12	-0.13	-0.12	-0.18
	IVC	1.02	1.03	1.04	1.01	1.03	8.29	8.91	9.00	8.26	8.63	-1.35	-1.46	-3.02	-2.34	-1.89
	HVC	0.98	1.00	1.01	0.99	1.03	7.92	8.63	8.78	7.59	7.70	-3.64	-2.46	-2.39	-2.64	-3.09
SP	Local	0.98	1.00	1.01	0.99	1.03	7.68	8.79	8.49	7.60	7.49	-3.33	-3.66	-2.55	-2.53	-2.50
	IVC	0.98	1.00	1.01	0.99	1.03	7.59	8.42	8.42	7.39	7.49	-20.68	-15.30	-10.37	-9.36	-7.75
	HVC	0.95	1.02	1.09	0.96	0.86	10.09	11.91	12.34	10.61	8.95	-0.07	-0.09	-0.02	0.15	0.07
SPC	Local	1.09	1.17	1.25	1.10	0.98	9.11	9.85	11.16	9.66	8.37	-0.92	-2.90	-1.99	-2.92	-2.25
	IVC	1.15	1.24	1.32	1.17	1.04	11.49	12.46	13.92	12.22	9.97	-4.70	1.98	4.32	-13.59	2.78
	HVC	0.98	1.00	1.01	0.94	0.06	11.15	12.45	12.13	11.64	0.72	0.11	0.05	0.02	0.17	0.18
SPIDER	Local	0.98	1.00	1.01	0.94	0.06	8.08	8.95	8.88	7.80	0.53	-0.22	-0.61	-0.40	-0.58	-0.80
	IVC	0.93	0.95	0.95	0.89	0.06	7.51	8.21	8.34	7.66	0.50	-10.58	-12.38	-10.13	-13.70	-11.68
	HVC	1.13	1.20	1.24	1.05	0.83	10.63	12.14	12.19	10.18	7.69	-0.09	0.07	0.09	0.09	-0.12
UMA	Local	1.11	1.18	1.22	1.04	0.82	10.26	10.77	11.16	9.25	7.39	-0.80	-1.27	-0.90	-1.00	-0.42
	IVC	1.13	1.20	1.24	1.06	0.83	9.33	10.14	10.41	8.59	6.51	-1.69	-1.58	1.16	0.41	-8.10
	HVC	1.10	1.21	1.31	1.01	0.97	7.14	7.87	9.02	6.34	6.02	-0.23	0.14	-0.37	-0.21	0.08
UMAEAST	Local	1.09	1.21	1.30	1.01	0.96	7.65	8.37	9.69	7.31	6.92	-0.76	-0.75	-0.66	-0.76	-0.72
	IVC	1.04	1.15	1.24	0.96	0.91	8.25	9.83	10.88	8.02	7.29	4.84	-3.59	5.45	-0.78	-4.92
	HVC	1.04	1.15	1.24	0.96	0.91	8.25	9.83	10.88	8.02	7.29	4.84	-3.59	5.45	-0.78	-4.92

Table B.2. Results from the Monte-Carlo simulations. $\delta_v = \langle \delta \epsilon'_v \rangle / \delta \epsilon_v$ is the ratio of the average statistical uncertainty of the emissivities estimated in the fits of the simulated data to the statistical uncertainty estimated in the fit of the actual data. A second ratio, with the same denominator, $\phi_v = \sigma(\epsilon'_v) / \delta \epsilon_v$, is the ratio of the standard deviation of the emissivities recovered in the simulations to the statistical uncertainty estimated in the fit of the actual data. The percentage bias in emissivity $b_v = 100((\epsilon'_v) - \epsilon_v) / \epsilon_v$.

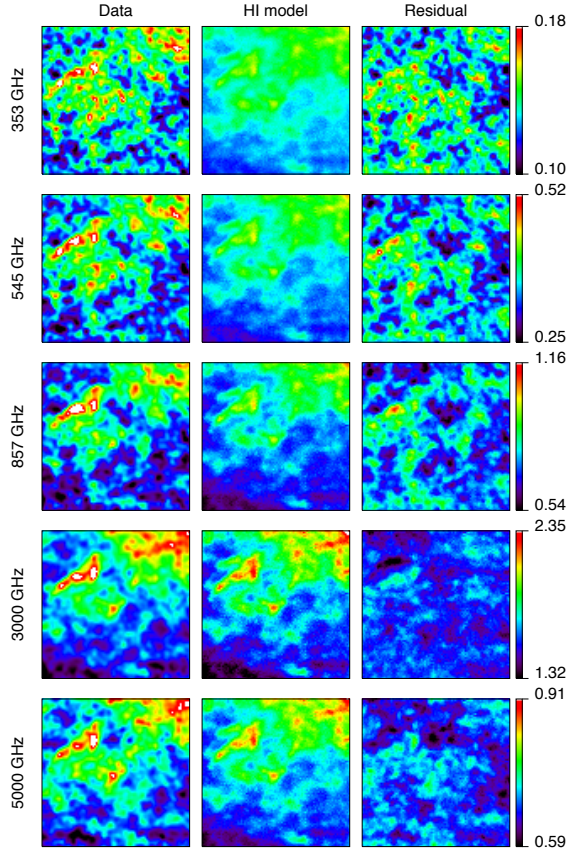


Fig. B.2. Like Fig. 2, for field AG.

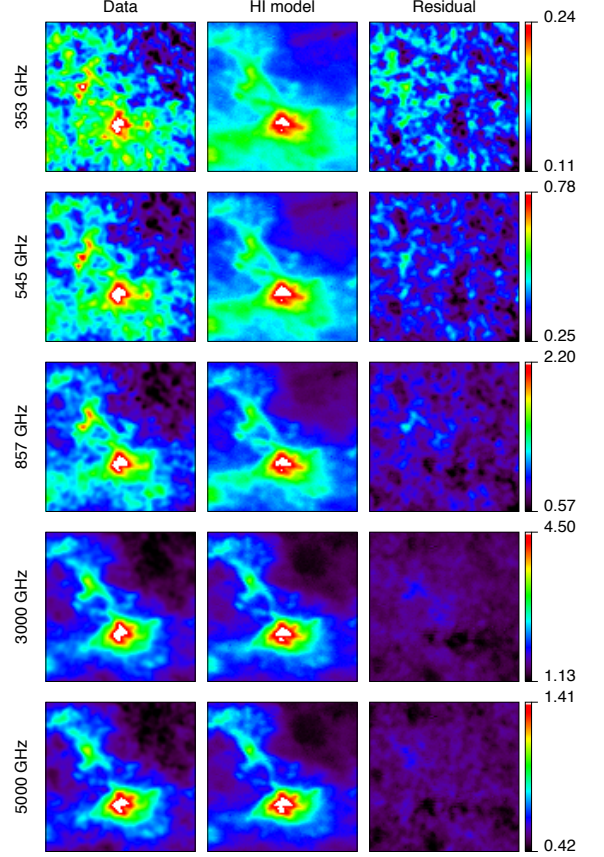


Fig. B.4. Like Fig. 2, for field G86.

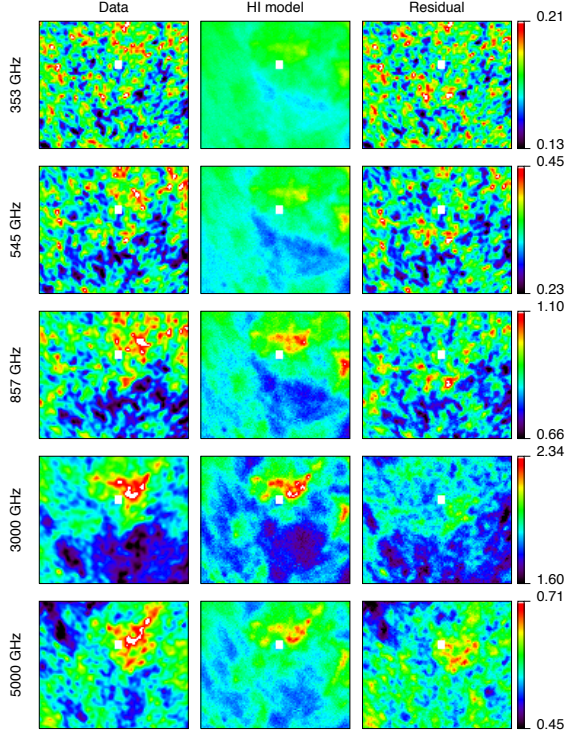


Fig. B.3. Like Fig. 2, for field MC.

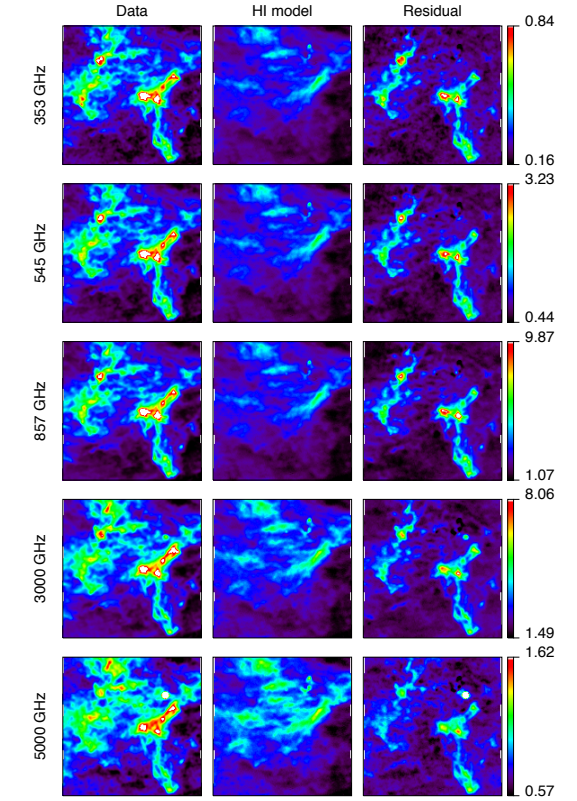


Fig. B.5. Like Fig. 2, for field UMA.

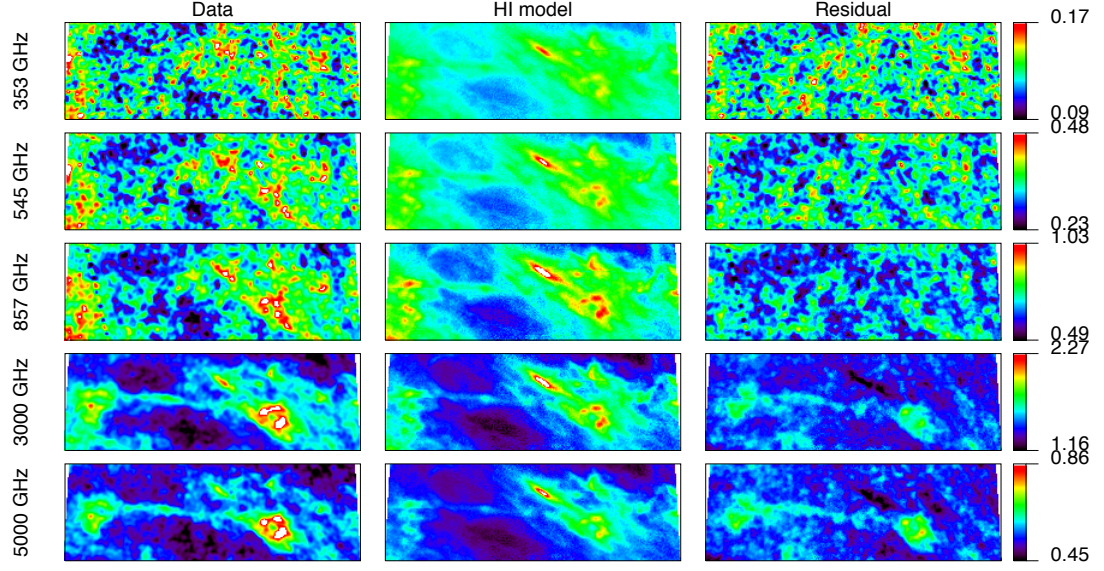


Fig. B.6. Like Fig. 2, for field BOOTES.

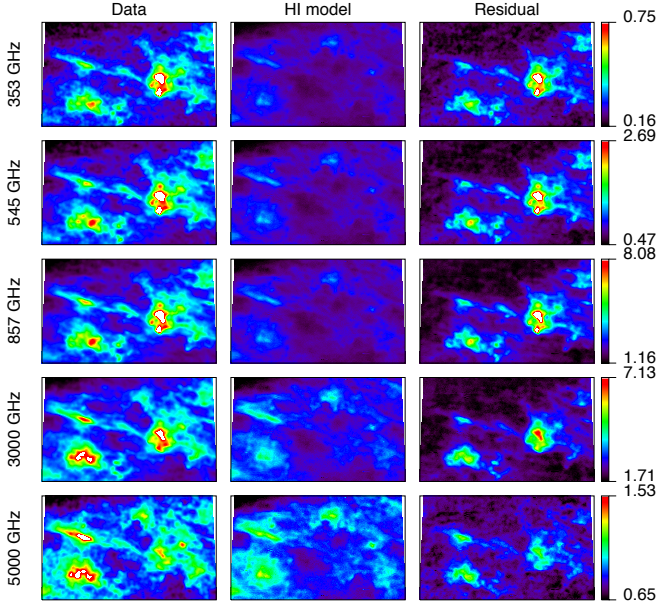


Fig. B.7. Like Fig. 2, for field UMAEAST.

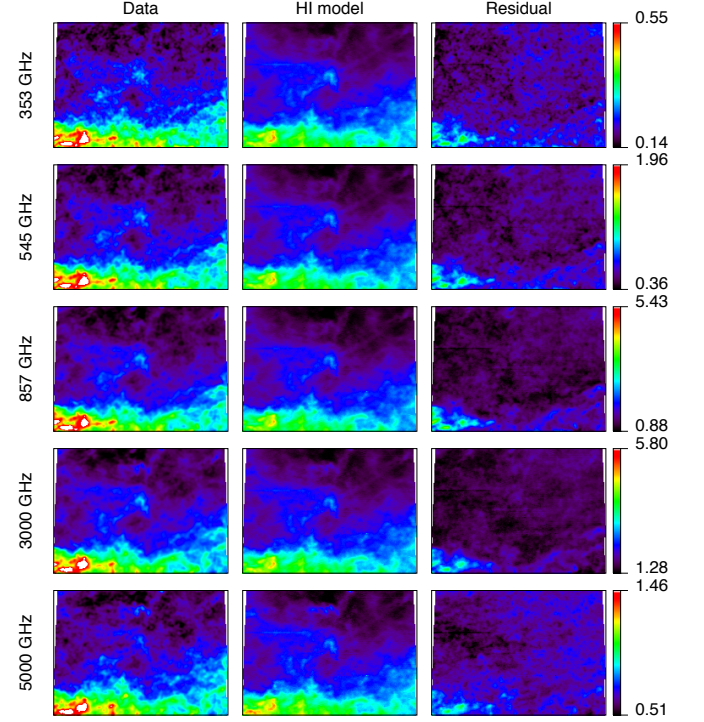


Fig. B.8. Like Fig. 2, for field SPC.

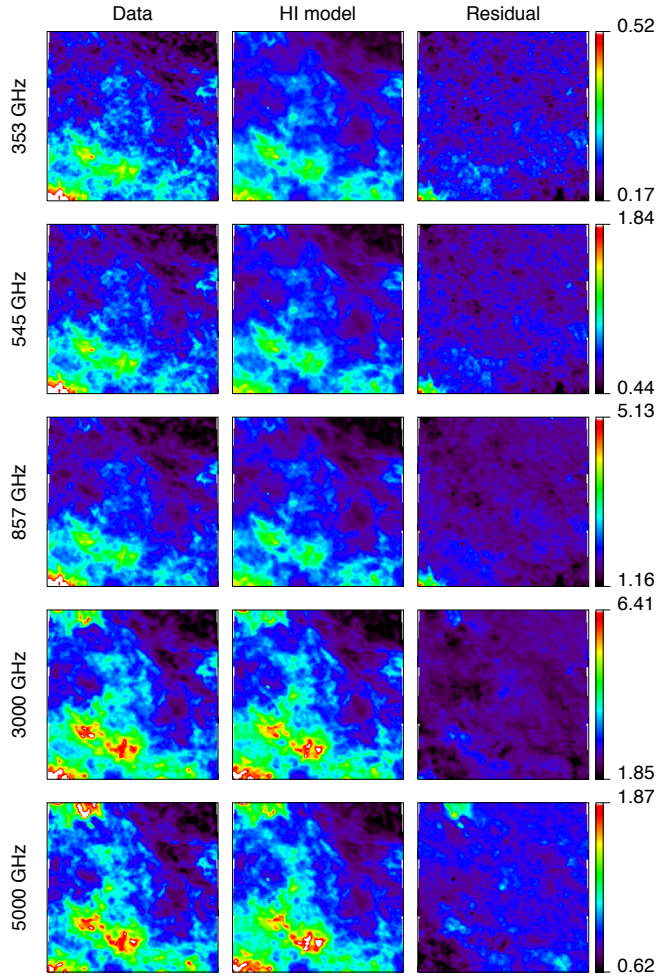


Fig. B.9. Like Fig. 2, for field NEP.

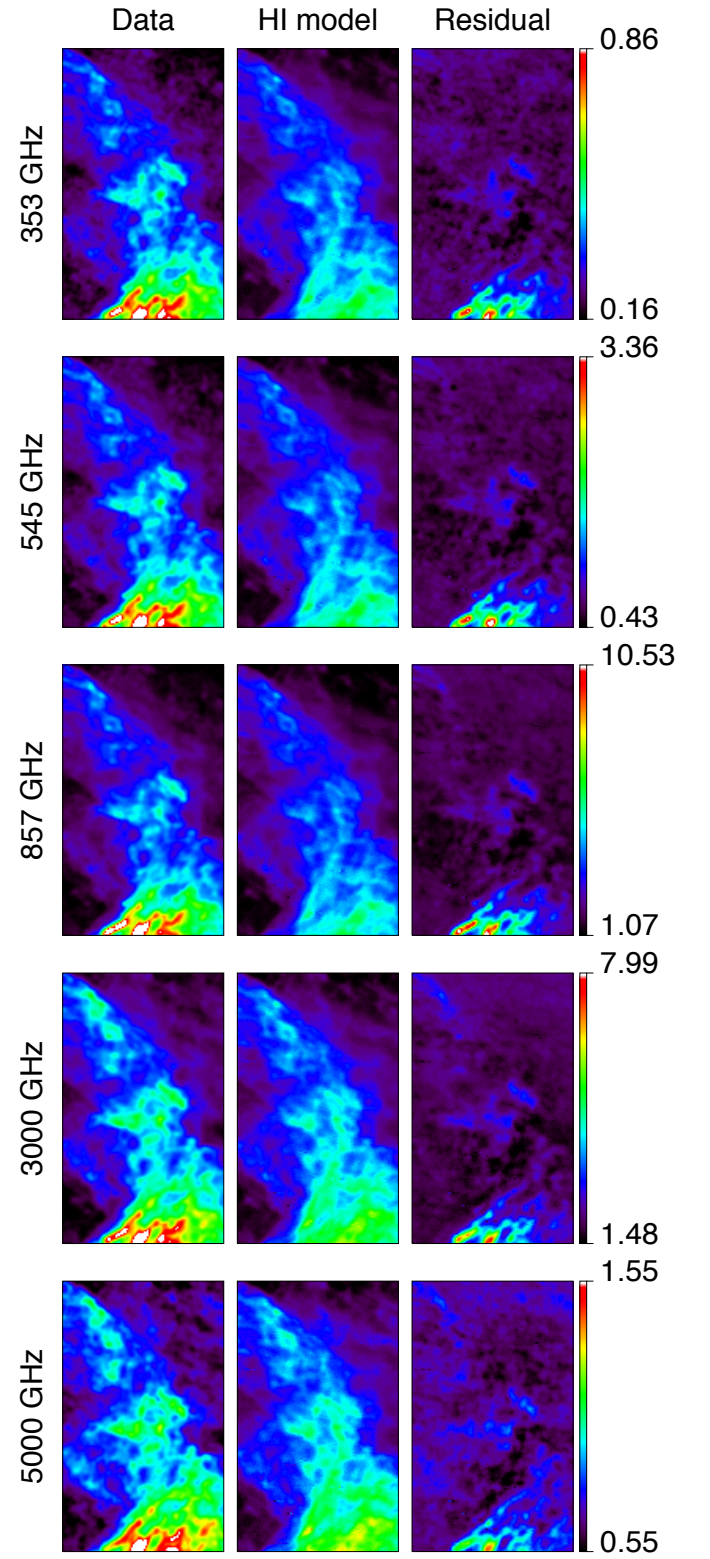


Fig. B.10. Like Fig. 2, for field POLNOR.

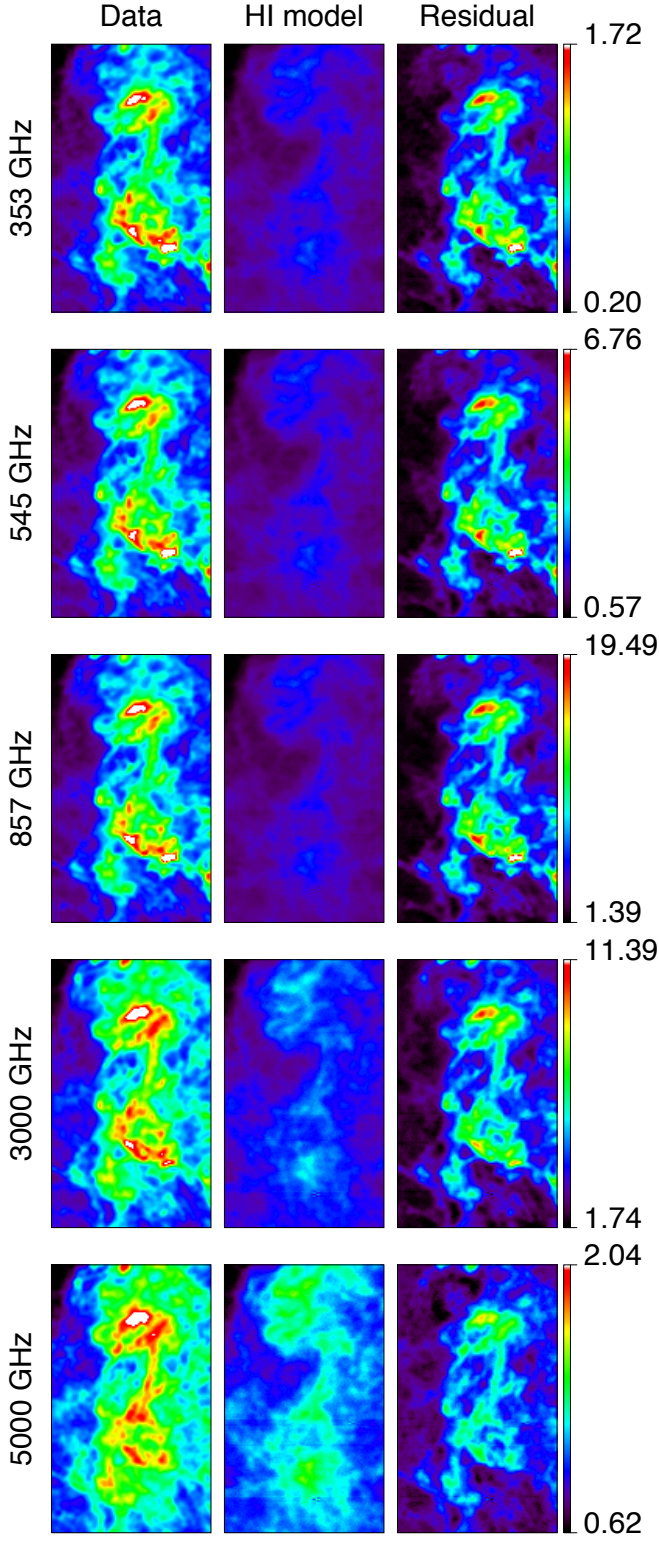


Fig. B.11. Like Fig. 2, for field POL.

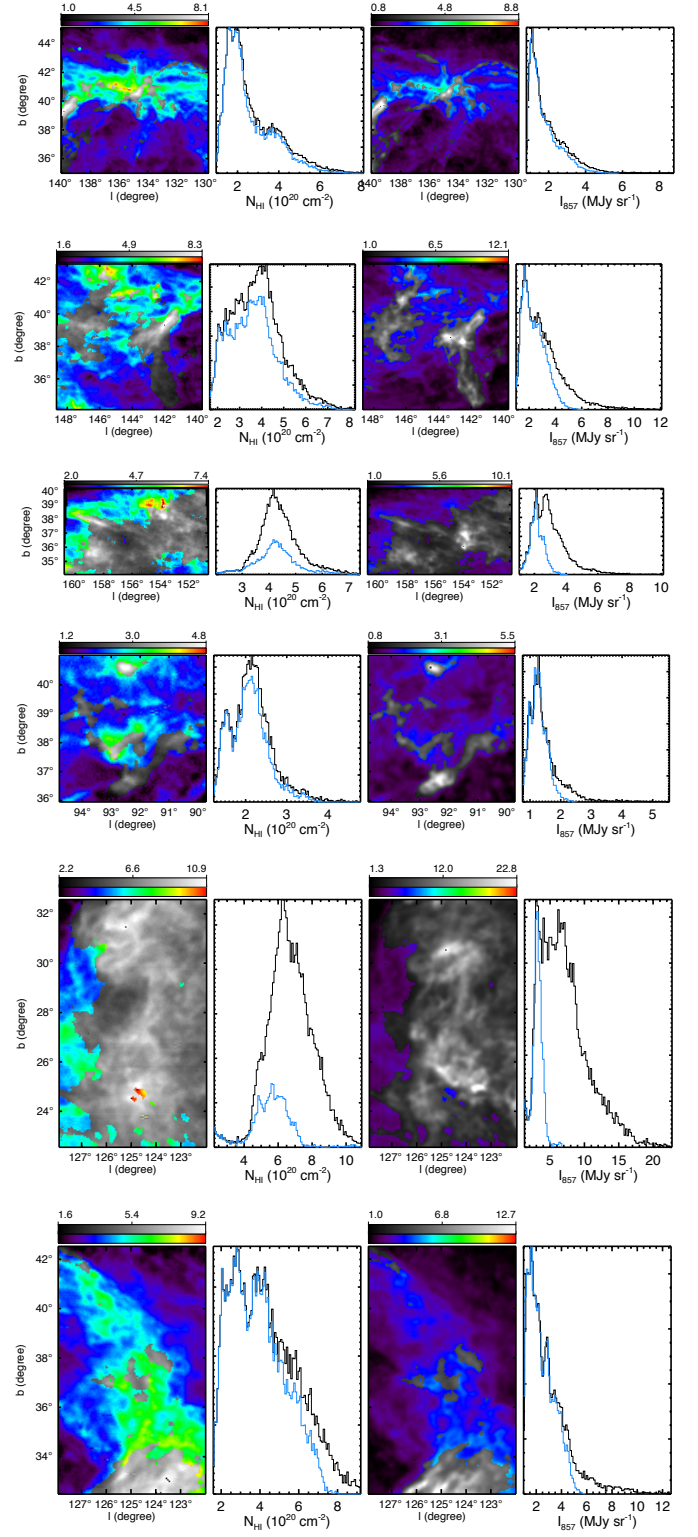


Fig. B.12. From top to bottom (percentage of pixels in the masks): SPIDER (90%), UMA (75%), UMAEAST (41%), DRACO (83%), POL (20%) and POLNOR (86%). Left image is the total HI integrated emission (units are 10^{20} cm^{-2}). Right image is the *Planck* 857 GHz map (units are MJy sr^{-1}). The histograms give the PDF of each map (all pixels in black, pixels kept in the mask in blue).

References

- Arendt, R. G., Odegard, N., Weiland, J. L., Sodroski, T. J., Hauser, M. G., Dwek, E., Kelsall, T., Moseley, S. H., Silverberg, R. F., Leisawitz, D., Mitchell, K., Reach, W. T. & Wright, E. L. 1998, *ApJ*, 508, 74.
- Barriault, L., Joncas, G., Falgarone, E., Marshall, D. J., Heyer, M., Boulanger, F., Foster, T., Brunt, C., Miville-Deschênes, M. A., Blagrove, K., Kothers, R., Landecker, T. L., Martin, P. G., Scott, D., Stil, J. M. & Taylor, A. R. 2010, *MNRAS*, 859, 859.
- Bersanelli, M., Mandolesi, N., Butler, R. C., Mennella, A., Villa, F., Aja, B., Artal, E., Artina, E., Baccigalupi, C., Balasini, M., Baldan, G., Banday, A., Bastia, P., Battaglia, P., Bernardino, T., Blackhurst, E., Boschini, L., Burigana, C., Cafagna, G., Cappellini, B., Cavaliere, F., Colombo, F., Crone, G., Cuttaia, F., D'Arcangelo, O., Danese, L., Davies, R. D., Davis, R. J., de Angelis, L., de Gasperis, G. C., de La Fuente, L., de Rosa, A., de Zotti, G., Falvella, M. C., Ferrari, F., Ferretti, R., Figini, L., Fogliani, S., Franceschet, C., Franceschi, E., Gaier, T., Garavaglia, S., Gomez, F., Gorski, K., Gregorio, A., Guzzi, P., Herreros, J. M., Hildebrandt, S. R., Hoyland, R., Hughes, N., Janssen, M., Jukkala, P., Kettle, D., Kilpiä, V. H., Laaninen, M., Lapolla, P. M., Lawrence, C. R., Lawson, D., Leahy, J. P., Leonardi, R., Leutenegger, P., Levin, S., Lilje, P. B., Lowe, S. R., Lubin, P. M., Maino, D., Malaspina, M., Maris, M., Marti-Canales, J. A., Martínez-Gonzalez, E., Mediavilla, A., Meinhold, P., Miccolis, M., Morgante, G., Natoli, P., Nesti, R., Pagan, L., Paine, C., Partridge, B., Pascual, J. P., Pasian, F., Pearson, D., Pecora, M., Perrotta, F., Platania, P., Pospieszalski, M., Poutanen, T., Prina, M., Rebolo, R., Roddis, N., Rubiño-Martin, J. A., Salmon, M. J., Sandri, M., Seiffert, M., Silvestri, R., Simonetto, A., Sjoman, P., Smoot, G. F., Sozzi, C., Stringhetti, L., Taddei, E., Tauber, J., Terenzi, L., Tomasi, M., Tuovinen, J., Valenziano, L., Varis, J., Vittorio, N., Wade, L. A., Wilkinson, A., Winder, F., Zacchei, A. & Zonca, A. September 2010, *A&A*, 520, A4+.
- Blagrove, K., Lockman, F. J. & Martin, P. G. Targeted deep surveys of high galactic latitude hi with the gbt. *arXiv:1009.0715*, 2010.
- Boothroyd, A., Blagrove, K., Lockman, F., Martin, P. & Pinheiro Gonçalves, D. 2011, *A&A*, in prep.
- Boulanger, F. & Pérou, M. 1988, *ApJ*, 330, 964.
- Boulanger, F., Abergel, A., Bernard, J. P., Burton, W. B., Desert, F. X., Hartmann, D., Lagache, G. & Puget, J. L. 1996, *A&A*, 312, 256.
- Calabretta, M. R. & Greisen, E. W. 2002, *A&A*, 395, 1077–1122.
- Collins, J. A., Shull, J. M. & Giroux, M. L. 2007, *ApJ*, 657, 271.
- Compiegne, M., Verstraete, L., Jones, A., Bernard, J. J. P., Boulanger, F., Flagey, N., Le Bourlot, J., Paradis, D. & Ysard, N. The global dust sed: Tracing the nature and evolution of dust with dustem. *arXiv:1010.2769*, 2010.
- Désert, F. X., Macías-Pérez, J. F., Mayet, F., Giardino, G., Renault, C., Aumont, J., Benoît, A., Bernard, J. P., Ponthieu, N. & Tristram, M. 2008, *A&A*, 481, 411–421.
- Dupac, X., Bernard, J. P., Boudet, N., Giard, M., Lamarre, J. M., Mény, C., Pajot, F., Ristorcelli, I., Serra, G., Stepnik, B. & Torre, J. P. 2003, *A&A*, 404, L11.
- Field, G. B., Goldsmith, D. W. & Habing, H. J. 1969, *ApJ*, 155, L149.
- Field, G. B. 1965, *ApJ*, 142, 531.
- Fixsen, D. J., Dwek, E., Mather, J. C., Bennett, C. L. & Shafer, R. A. 1998, *ApJ*, 508, 123.
- Gaensler, B. M., Madsen, G. J., Chatterjee, S. & Mao, S. A. 2008, *PASA*, 25, 184–200.
- Gillmon, K., Shull, J. M., Tumlinson, J. & Danforth, C. 2006, *ApJ*, 636, 891–907.
- Gorski, K. M., Hivon, E., Banday, A. J., Wandelt, B. D., Hansen, F. K., Reinecke, M. & Bartelmann, M. 2005, *ApJ*, 622, 759–771.
- Heiles, C. & Troland, T. H. 2003, *ApJ*, 586, 1067.
- Herbstmeier, U., Heithausen, A. & Mebold, U. 1993, *A&A*, 272, 514.
- Ingalls, J. G., Miville-Deschênes, M. A., Reach, W. T., Noriega-Crespo, A., Carey, S. J., Boulanger, F., Stolovy, S. R., Padgett, D. L., Burgdorf, M. J., Fajardo-Acosta, S. B., Glaccum, W. J., Helou, G., Hoard, D. W., Karr, J., O'Linger, J., Rebull, L. M., Rho, J., Stauffer, J. R. & Wachter, S. 2004, *ApJS*, 154, 281–285.
- Jenkins, E. B. 2009, *ApJ*, 700, 1299.
- Joncas, G., Boulanger, F. & Dewdney, P. E. 1992, *ApJ*, 397, 165.
- Jones, M. H., Rowan-Robinson, M., Branduardi-Raymont, G., Smith, P., Pedlar, A. & Willacy, K. 1995, *MNRAS*, 277, 1587.
- Lagache, G., Haffner, L. M., Reynolds, R. J. & Tufte, S. L. 2000, *A&A*, 354, 247.
- Lagache, G., Bavouzet, N., Fernandez-Conde, N., Ponthieu, N., Rodet, T., Dole, H., Miville-Deschênes, M. A. & Puget, J. L. 2007, *ApJ*, 665, L89.
- Lamarre, J., Puget, J., Ade, P. A. R., Bouchet, F., Guyot, G., Lange, A. E., Pajot, F., Arondel, A., Benabed, K., Beney, J., Benoît, A., Bernard, J., Bhatia, R., Blanc, Y., Bock, J. J., Bréelle, E., Bradshaw, T. W., Camus, P., Catalano, A., Charra, J., Charra, M., Church, S. E., Couchot, F., Coulais, A., Crill, B. P., Crook, M. R., Dassas, K., de Bernardis, P., Delabrouille, J., de Marillac, P., Delouis, J., Désert, F., Dumesnil, C., Dupac, X., Efstathiou, G., Eng, P., Evesque, C., Fourmond, J., Ganga, K., Giard, M., Gispert, R., Guglielmi, L., Haissinski, J., Henrot-Versillé, S., Hivon, E., Holmes, W. A., Jones, W. C., Koch, T. C., Lagardère, H., Lami, P., Landé, J., Leriche, B., Leroy, C., Longval, Y., Macías-Pérez, J. F., Maciaszek, T., Maffei, B., Mansoux, B., Marty, C., Masi, S., Mercier, C., Miville-Deschênes, M., Moneti, A., Montier, L., Murphy, J. A., Narbonne, J., Nexon, M., Paine, C. G., Pahn, J., Perdereau, O., Piacentini, F., Piat, M., Plaszczyński, S., Pointecouteau, E., Pons, R., Ponthieu, N., Prunet, S., Rambaud, D., Recouvreur, G., Renault, C., Ristorcelli, I., Rosset, C., Santos, D., Savini, G., Serra, G., Stassi, P., Sudiwala, R. V., Sygnet, J., Tauber, J. A., Torre, J., Tristram, M., Vibert, L., Woodcraft, A., Yurchenko, V. & Yvon, D. September 2010, *A&A*, 520, A9+.
- Lockman, F. J. & Condon, J. J. 2005, *AJ*, 129, 1968–1977.
- Low, F. J., Young, E., Beintema, D. A., Gautier, T. N., Beichman, C. A., Aumann, H. H., Gillett, F. C., Neugebauer, G., Boggess, N. & Emerson, J. P. 1984, *ApJ*, 278, L19.
- Mandolesi, N., Bersanelli, M., Butler, R. C., Artal, E., Baccigalupi, C., Balbi, A., Banday, A. J., Barreiro, R. B., Bartelmann, M., Bennett, K., Bhandari, P., Bonaldi, A., Borrill, J., Bremer, M., Burigana, C., Bowman, R. C., Cabella, P., Cantalupo, C., Cappellini, B., Courvoisier, T., Crone, G., Cuttaia, F., Danese, L., D'Arcangelo, O., Davies, R. D., Davis, R. J., de Angelis, L., de Gasperis, G., de Rosa, A., de Troia, G., de Zotti, G., Dick, J., Dickinson, C., Diego, J. M., Donzelli, S., Dörl, U., Dupac, X., Enßlin, T. A., Eriksen, H. K., Falvella, M. C., Feinelli, F., Frailis, M., Franceschi, E., Gaier, T., Galeotta, S., Gasparo, F., Giardino, G., Gomez, F., Gonzalez-Nuevo, J., Górski, K. M., Gregorio, A., Gruppiso, A., Hansen, F., Hell, R., Herranz, D., Herreros, J. M., Hildebrandt, S., Hovest, W., Hoyland, R., Hufferberger, K., Janssen, M., Jaffe, T., Kihänen, E., Keskitalo, R., Kisner, T., Kurki-Suonio, H., Lähteenmäki, A., Lawrence, C. R., Leach, S. M., Leahy, J. P., Leonardi, R., Levin, S., Lilje, P. B., López-Caniego, M., Lowe, S. R., Lubin, P. M., Maino, D., Malaspina, M., Maris, M., Marti-Canales, J., Martínez-Gonzalez, E., Massardi, M., Matarrese, S., Matthai, F., Meinhold, P., Melchiorri, A., Mendes, L., Mennella, A., Morgante, G., Morigi, G., Morisset, N., Moss, A., Nash, A., Natoli, P., Nesti, R., Paine, C., Partridge, B., Pasian, F., Passvogel, T., Pearson, D., Pérez-Cuevas, L., Perrotta, F., Polenta, G., Popa, L. A., Poutanen, T., Prezeau, G., Prina, M., Rachen, J. P., Rebolo, R., Reinecke, M., Ricciardi, S., Riller, T., Rocha, G., Roddis, N., Rohlf, R., Rubiño-Martin, J. A., Salerno, E., Sandri, M., Scott, D., Seiffert, M., Silk, J., Simonetto, A., Smoot, G. F., Sozzi, C., Sternberg, J., Stivoli, F., Stringhetti, L., Tauber, J., Terenzi, L., Tomasi, M., Tuovinen, J., Türlér, M., Valenziano, L., Varis, J., Vielva, P., Villa, F., Vittorio, N., Wade, L., White, M., White, S., Wilkinson, A., Zacchei, A. & Zonca, A. September 2010, *A&A*, 520, A3+.
- Martin, P. G., Rogers, C., Reach, W. T., Dewdney, P. E. & Heiles, C. E. Arcminute scale hi and iras observations toward the high latitude cloud g86.5+59.6. In Cutri, R. & W.B. Latter, E. editors, *The First Symposium on the Infrared Cirrus and Diffuse Interstellar Clouds*, page 188, 1994.
- Martin, P. G., Miville-Deschênes, M. A., Roy, A., Bernard, J. P., Molinari, S., Billot, N., Brunt, C., Calzoletti, L., Digiorgio, A. M., Elia, D., Faustini, F., Joncas, G., Mottram, J. C., Natoli, P., Noriega-Crespo, A., Paladini, R., Robitaille, J. F., Strafella, F., Traficante, A. & Veneziani, M. 2010, *A&A*, 518, L105.
- Martin, P. G., Blagrove, K. P. M., Boothroyd, A. L., Lockman, F. J., Miville-Deschênes, M. A. & Pinheiro Gonçalves, D. C. 2011, *ApJ*, in prep.
- Mennella et al. 2011, *Planck early results 03: First assessment of the Low Frequency Instrument in-flight performance*. Submitted to *A&A*.
- Miville-Deschênes, M. A. & Lagache, G. 2005, *ApJS*, 157, 302–323.
- Miville-Deschênes, M. A., Boulanger, F., Joncas, G. & Falgarone, E. 2002a, *A&A*, 381, 209.
- Miville-Deschênes, M. A., Lagache, G. & Puget, J. L. 2002b, *A&A*, 393, 749.
- Miville-Deschênes, M. A., Boulanger, F., Reach, W. T. & Noriega-Crespo, A. 2005, *ApJ*, 631, L57–L60.
- Miville-Deschênes, M. A., Lagache, G., Boulanger, F. & Puget, J. L. 2007, *A&A*, 469, 595–605.
- Miville-Deschênes, M. A., Martin, P. G., Abergel, A., Bernard, J. P., Boulanger, F., Lagache, G., Anderson, L. D., André, P., Arab, H., Baluteau, J. P., Blagrove, K., Bontemps, S., Cohen, M., Compiegne, M., Cox, P., Dartois, E., Davis, G., Emery, R., Fulton, T., Gry, C., Habart, E., Huang, M., Joblin, C., Jones, S. C., Kirk, J., Lim, T., Madden, S., Makiwa, G., Menshchikov, A., Molinari, S., Moseley, H., Motte, F., Naylor, D. A., Okumura, K., Pinheiro Gonçalves, D., Polehampton, E., Rodón, J. A., Russeil, D., Saraceno, P., Schneider, N., Sidher, S., Spencer, L., Swinyard, B., Ward-Thompson, D., White, G. J. & Zavagno, A. 2010, *A&A*, 518, L104.
- Planck Collaboration. 2011a, *Planck early results 01: The Planck mission*. Submitted to *A&A*.
- Planck Collaboration. 2011b, *Planck early results 02: The thermal performance of Planck*. Submitted to *A&A*.
- Planck Collaboration. 2011c, *Planck early results 07: The Early Release Compact Source Catalogue*. Submitted to *A&A*.

- Planck Collaboration. 2011d, *Planck early results 08: The all-sky early Sunyaev-Zeldovich cluster sample*. Submitted to A&A.
- Planck Collaboration. 2011e, *Planck early results 09: XMM-Newton follow-up for validation of Planck cluster candidates*. Submitted to A&A.
- Planck Collaboration. 2011f, *Planck early results 10: Statistical analysis of Sunyaev-Zeldovich scaling relations for X-ray galaxy clusters*. Submitted to A&A.
- Planck Collaboration. 2011g, *Planck early results 11: Calibration of the local galaxy cluster Sunyaev-Zeldovich scaling relations*. Submitted to A&A.
- Planck Collaboration. 2011h, *Planck early results 12: Cluster Sunyaev-Zeldovich optical Scaling relations*. Submitted to A&A.
- Planck Collaboration. 2011i, *Planck early results 13: Statistical properties of extragalactic radio sources in the Planck Early Release Compact Source Catalogue*. Submitted to A&A.
- Planck Collaboration. 2011j, *Planck early results 14: Early Release Compact Source Catalogue validation and extreme radio sources*. Submitted to A&A.
- Planck Collaboration. 2011k, *Planck early results 15: Spectral energy distributions and radio continuum spectra of northern extragalactic radio sources*. Submitted to A&A.
- Planck Collaboration. 2011l, *Planck early results 16: The Planck view of nearby galaxies*. Submitted to A&A.
- Planck Collaboration. 2011m, *Planck early results 17: Origin of the submillimetre excess dust emission in the Magellanic Clouds*. Submitted to A&A.
- Planck Collaboration. 2011n, *Planck early results 18: The power spectrum of cosmic infrared background anisotropies*. Submitted to A&A.
- Planck Collaboration. 2011o, *Planck early results 19: All-sky temperature and dust optical depth from Planck and IRAS — constraints on the “dark gas” in our Galaxy*. Submitted to A&A.
- Planck Collaboration. 2011p, *Planck early results 20: New light on anomalous microwave emission from spinning dust grains*. Submitted to A&A.
- Planck Collaboration. 2011q, *Planck early results 21: Properties of the interstellar medium in the Galactic plane*. Submitted to A&A.
- Planck Collaboration. 2011r, *Planck early results 22: The submillimetre properties of a sample of Galactic cold clumps*. Submitted to A&A.
- Planck Collaboration. 2011s, *Planck early results 23: The Galactic cold core population revealed by the first all-sky survey*. Submitted to A&A.
- Planck Collaboration. 2011t, *Planck early results 24: Dust in the diffuse interstellar medium and the Galactic halo*. Submitted to A&A.
- Planck Collaboration. 2011u, *Planck early results 25: Thermal dust in nearby molecular clouds*. Submitted to A&A.
- Planck Collaboration. 2011v, *The Explanatory Supplement to the Planck Early Release Compact Source Catalogue*. ESA.
- Planck HFI Core Team. 2011a, *Planck early results 04: First assessment of the High Frequency Instrument in-flight performance*. Submitted to A&A.
- Planck HFI Core Team. 2011b, *Planck early results 06: The High Frequency Instrument data processing*. Submitted to A&A.
- Press, W. H., Teukolsky, S. A., Vetterling, W. T. & Flannery, B. P. 1995, *Numerical Recipes in C*. Cambridge University Press.
- Rachford, B. L., Snow, T. P., Tumlinson, J., Shull, J. M., Blair, W. P., Ferlet, R., Friedman, S. D., Gry, C., Jenkins, E. B., Morton, D. C., Savage, B. D., Sonnentrucker, P., Vidal-Madjar, A., Welty, D. E. & York, D. G. 2002, *ApJ*, 577, 221.
- Rachford, B. L., Snow, T. P., Destree, J. D., Ross, T. L., Ferlet, R., Friedman, S. D., Gry, C., Jenkins, E. B., Morton, D. C., Savage, B. D., Shull, J. M., Sonnentrucker, P., Tumlinson, J., Vidal-Madjar, A., Welty, D. E. & York, D. G. 2009, *ApJS*, 180, 125–137.
- Reach, W. T., Koo, B. C. & Heiles, C. 1994, *ApJ*, 429, 672.
- Reach, W. T., Wall, W. F. & Odegard, N. 1998, *ApJ*, 507, 507.
- Reynolds, R. J. 1989, *ApJ*, 339, L29.
- Savage, B. D., Drake, J. F., Budich, W. & Bohlin, R. C. 1977, *ApJ*, 216, 291.
- Shetty, R., Kauffmann, J., Schnee, S., Goodman, A. A. & Ercolano, B. 2009, *ApJ*, 696, 2234.
- Spitzer, L. 1956, *ApJ*, 124, 20.
- Stepnik, B., Abergel, A., Bernard, J. P., Boulanger, F., Cambrésy, L., Giard, M., Jones, A. P., Lagache, G., Lamarre, J. M., Meny, C., Pajot, F., Peintre, F. L., Ristorcelli, I., Serra, G. & Torre, J. P. 2003, *A&A*, 398, 551.
- Tauber, J. A., Mandolesi, N., Puget, J., Banos, T., Bersanelli, M., Bouchet, F. R., Butler, R. C., Charra, J., Crone, G., Dodsworth, J. & et al. September 2010, *A&A*, 520, A1+.
- Veneziani, M., Ade, P. A. R., Bock, J. J., Boscaleri, A., Crill, B. P., de Bernardis, P., de Gasperis, G., de Oliveira-Costa, A., de Troia, G., Di Stefano, G., Ganga, K. M., Jones, W. C., Kisner, T. S., Lange, A. E., Mactavish, C. J., Masi, S., Maukopf, P. D., Montroy, T. E., Natoli, P., Netterfield, C. B., Pascale, E., Piacentini, F., Pietrobon, D., Polenta, G., Ricciardi, S., Romeo, G. & Ruhl, J. E. 2010, *ApJ*, 713, 959.
- Wakker, B. P. 2006, *ApJS*, 163, 282–305.
- Wheelock, S., Gautier, T. N., Chillemi, J., Kester, D., McCallon, H., Oken, C., White, J., Gregorich, D., Boulanger, F., Good, J. & Chester, T. Issa explanatory supplement. Technical report, Page:, 1993.
- Witt, A. N., Gold, B., Barnes, F. S., Deroo, C. T., Vijh, U. P. & Madsen, G. J. 2010, *ApJ*, 724, 1551.
- Zacchei et al. 2011, *Planck early results 05: The Low Frequency Instrument data processing*. Submitted to A&A.
-
- ¹ Aalto University Metsähovi Radio Observatory, Metsähovintie 114, FIN-02540 Kylmälä, Finland
- ² Agenzia Spaziale Italiana Science Data Center, c/o ESRIN, via Galileo Galilei, Frascati, Italy
- ³ Astroparticule et Cosmologie, CNRS (UMR7164), Université Denis Diderot Paris 7, Bâtiment Condorcet, 10 rue A. Domon et Léonie Duquet, Paris, France
- ⁴ Atacama Large Millimeter/submillimeter Array, ALMA Santiago Central Offices Alonso de Cordova 3107, Vitacura, Casilla 763 0355, Santiago, Chile
- ⁵ CITA, University of Toronto, 60 St. George St., Toronto, ON M5S 3H8, Canada
- ⁶ CNRS, IRAP, 9 Av. colonel Roche, BP 44346, F-31028 Toulouse cedex 4, France
- ⁷ California Institute of Technology, Pasadena, California, U.S.A.
- ⁸ DAMTP, Centre for Mathematical Sciences, Wilberforce Road, Cambridge CB3 0WA, U.K.
- ⁹ DSM/Irfu/SPP, CEA-Saclay, F-91191 Gif-sur-Yvette Cedex, France
- ¹⁰ DTU Space, National Space Institute, Juliane Mariesvej 30, Copenhagen, Denmark
- ¹¹ Département de physique, de génie physique et d’optique, Université Laval, Québec, Canada
- ¹² Departamento de Física, Universidad de Oviedo, Avda. Calvo Sotelo s/n, Oviedo, Spain
- ¹³ Department of Astronomy and Astrophysics, University of Toronto, 50 Saint George Street, Toronto, Ontario, Canada
- ¹⁴ Department of Physics & Astronomy, University of British Columbia, 6224 Agricultural Road, Vancouver, British Columbia, Canada
- ¹⁵ Department of Physics, Gustaf Hållströmin katu 2a, University of Helsinki, Helsinki, Finland
- ¹⁶ Department of Physics, Princeton University, Princeton, New Jersey, U.S.A.
- ¹⁷ Department of Physics, Purdue University, 525 Northwestern Avenue, West Lafayette, Indiana, U.S.A.
- ¹⁸ Department of Physics, University of California, Berkeley, California, U.S.A.
- ¹⁹ Department of Physics, University of California, One Shields Avenue, Davis, California, U.S.A.
- ²⁰ Department of Physics, University of California, Santa Barbara, California, U.S.A.
- ²¹ Department of Physics, University of Illinois at Urbana-Champaign, 1110 West Green Street, Urbana, Illinois, U.S.A.

- 22 Dipartimento di Fisica G. Galilei, Università degli Studi di Padova, via Marzolo 8, 35131 Padova, Italy
- 23 Dipartimento di Fisica, Università La Sapienza, P. le A. Moro 2, Roma, Italy
- 24 Dipartimento di Fisica, Università degli Studi di Milano, Via Celoria, 16, Milano, Italy
- 25 Dipartimento di Fisica, Università degli Studi di Trieste, via A. Valerio 2, Trieste, Italy
- 26 Dipartimento di Fisica, Università di Roma Tor Vergata, Via della Ricerca Scientifica, 1, Roma, Italy
- 27 Discovery Center, Niels Bohr Institute, Blegdamsvej 17, Copenhagen, Denmark
- 28 Dpto. Astrofísica, Universidad de La Laguna (ULL), E-38206 La Laguna, Tenerife, Spain
- 29 European Southern Observatory, ESO Vitacura, Alonso de Cordova 3107, Vitacura, Casilla 19001, Santiago, Chile
- 30 European Space Agency, ESAC, Planck Science Office, Camino bajo del Castillo, s/n, Urbanización Villafranca del Castillo, Villanueva de la Cañada, Madrid, Spain
- 31 European Space Agency, ESTEC, Keplerlaan 1, 2201 AZ Noordwijk, The Netherlands
- 32 Green Bank, West Virginia, NRAO, P.O. Box 2, Rt. 28/92, Green Bank, WV 24944-0002, U.S.A.
- 33 Helsinki Institute of Physics, Gustaf Hållströmin katu 2, University of Helsinki, Helsinki, Finland
- 34 INAF - Osservatorio Astrofisico di Catania, Via S. Sofia 78, Catania, Italy
- 35 INAF - Osservatorio Astronomico di Padova, Vicolo dell'Osservatorio 5, Padova, Italy
- 36 INAF - Osservatorio Astronomico di Roma, via di Frascati 33, Monte Porzio Catone, Italy
- 37 INAF - Osservatorio Astronomico di Trieste, Via G.B. Tiepolo 11, Trieste, Italy
- 38 INAF/IASF Bologna, Via Gobetti 101, Bologna, Italy
- 39 INAF/IASF Milano, Via E. Bassini 15, Milano, Italy
- 40 INRIA, Laboratoire de Recherche en Informatique, Université Paris-Sud 11, Bâtiment 490, 91405 Orsay Cedex, France
- 41 IPAG: Institut de Planétologie et d'Astrophysique de Grenoble, Université Joseph Fourier, Grenoble 1 / CNRS-INSU, UMR 5274, Grenoble, F-38041, France
- 42 Imperial College London, Astrophysics group, Blackett Laboratory, Prince Consort Road, London, SW7 2AZ, U.K.
- 43 Infrared Processing and Analysis Center, California Institute of Technology, Pasadena, CA 91125, U.S.A.
- 44 Institut d'Astrophysique Spatiale, CNRS (UMR8617) Université Paris-Sud 11, Bâtiment 121, Orsay, France
- 45 Institut d'Astrophysique de Paris, CNRS UMR7095, Université Pierre & Marie Curie, 98 bis boulevard Arago, Paris, France
- 46 Institute of Astronomy and Astrophysics, Academia Sinica, Taipei, Taiwan
- 47 Institute of Theoretical Astrophysics, University of Oslo, Blindern, Oslo, Norway
- 48 Instituto de Astrofísica de Canarias, C/Vía Láctea s/n, La Laguna, Tenerife, Spain
- 49 Instituto de Física de Cantabria (CSIC-Universidad de Cantabria), Avda. de los Castros s/n, Santander, Spain
- 50 Jet Propulsion Laboratory, California Institute of Technology, 4800 Oak Grove Drive, Pasadena, California, U.S.A.
- 51 Jodrell Bank Centre for Astrophysics, Alan Turing Building, School of Physics and Astronomy, The University of Manchester, Oxford Road, Manchester, M13 9PL, U.K.
- 52 Kavli Institute for Cosmology Cambridge, Madingley Road, Cambridge, CB3 0HA, U.K.
- 53 LERMA, CNRS, Observatoire de Paris, 61 Avenue de l'Observatoire, Paris, France
- 54 Laboratoire AIM, IRFU/Service d'Astrophysique - CEA/DSM - CNRS - Université Paris Diderot, Bât. 709, CEA-Saclay, F-91191 Gif-sur-Yvette Cedex, France
- 55 Laboratoire Traitement et Communication de l'Information, CNRS (UMR 5141) and Télécom ParisTech, 46 rue Barrault F-75634 Paris Cedex 13, France
- 56 Laboratoire de Physique Subatomique et de Cosmologie, CNRS, Université Joseph Fourier Grenoble I, 53 rue des Martyrs, Grenoble, France
- 57 Laboratoire de l'Accélérateur Linéaire, Université Paris-Sud 11, CNRS/IN2P3, Orsay, France
- 58 Lawrence Berkeley National Laboratory, Berkeley, California, U.S.A.
- 59 Max-Planck-Institut für Astrophysik, Karl-Schwarzschild-Str. 1, 85741 Garching, Germany
- 60 MilliLab, VTT Technical Research Centre of Finland, Tietotie 3, Espoo, Finland
- 61 National University of Ireland, Department of Experimental Physics, Maynooth, Co. Kildare, Ireland
- 62 Niels Bohr Institute, Blegdamsvej 17, Copenhagen, Denmark
- 63 Observational Cosmology, Mail Stop 367-17, California Institute of Technology, Pasadena, CA, 91125, U.S.A.
- 64 Optical Science Laboratory, University College London, Gower Street, London, U.K.
- 65 SISSA, Astrophysics Sector, via Bonomea 265, 34136, Trieste, Italy
- 66 SUPA, Institute for Astronomy, University of Edinburgh, Royal Observatory, Blackford Hill, Edinburgh EH9 3HJ, U.K.

⁶⁷ School of Physics and Astronomy, Cardiff University, Queens Buildings, The Parade, Cardiff, CF24 3AA, U.K.

⁶⁸ Space Sciences Laboratory, University of California, Berkeley, California, U.S.A.

⁶⁹ Spitzer Science Center, 1200 E. California Blvd., Pasadena, California, U.S.A.

⁷⁰ Stanford University, Dept of Physics, Varian Physics Bldg, 382 Via Pueblo Mall, Stanford, California, U.S.A.

⁷¹ Université de Toulouse, UPS-OMP, IRAP, F-31028 Toulouse cedex 4, France

⁷² Universities Space Research Association, Stratospheric Observatory for Infrared Astronomy, MS 211-3, Moffett Field, CA 94035, U.S.A.

⁷³ University of Cambridge, Cavendish Laboratory, Astrophysics group, JJ Thomson Avenue, Cambridge, U.K.

⁷⁴ University of Cambridge, Institute of Astronomy, Madingley Road, Cambridge, U.K.

⁷⁵ University of Granada, Departamento de Física Teórica y del Cosmos, Facultad de Ciencias, Granada, Spain

⁷⁶ University of Miami, Knight Physics Building, 1320 Campo Sano Dr., Coral Gables, Florida, U.S.A.

⁷⁷ Warsaw University Observatory, Aleje Ujazdowskie 4, 00-478 Warszawa, Poland